OEA | Opto-Electronic Advances

Review

March 2026, Vol. 9, No. 3

Open Access

Emerging landscape of photonic bound states in the continuum for next-generation metadevices

Thi Thu Ha Do[1†], Ronghui Lin[1†], Daniil A. Shilkin[1], Zhiyi Yuan[1,2,3], Cuong Dang[2,3], Arseniy I. Kuznetsov[1], Jinghua Teng[1]* and Son Tung Ha[1]*

Abstract: Bound states in the continuum (BICs) have emerged at the forefront of optics and nanophotonics due to their exceptionally high quality-factors and unique topological characteristics. Advances in design capabilities, nanofabrication and characterization have enabled precise control of BIC resonances at subwavelength scale, unlocking exciting opportunities for applications in diverse areas such as lasing, optical sensing and nonlinear optics. The integration of phase-change materials and liquid crystals has facilitated dynamic control over light emission and absorption. In this Review, we provide a comprehensive overview of the latest progress in BIC research, covering both foundational concepts and recent advances. We begin with the underlying physics and highlight emerging design strategies, including machine learning and inverse design approaches. We discuss major breakthroughs in super-BICs, chiral BICs, intriguing concepts of flatband BICs and Moiré BICs, along with exotic phenomena, such as strong light-matter interaction, ultrafast dynamics and exceptional points. We further review the recent advancements and key challenges in BIC-enabled applications. Finally, we offer our perspectives on the promising future of BIC in fundamental research emphasizing emerging directions such as multilayer metasurfaces, interfacing BICs with quantum emitters, new capabilities enabled by advanced fabrication and design, and pathways towards scalable integration into photonic BIC metadevices.

Keywords: bound state in the continuum; metasurfaces; meta-devices; nanophotonics; optoelectronics

DOI: 10.29026/oea.2026.250224 | CSTR: 32247.14.oea.2026.250224

Citation: Do TTH, Lin RH, Shilkin DA et al. Emerging landscape of photonic bound states in the continuum for next-generation metadevices. *Opto-Electron Adv* **9**, 250224 (2026).

1 Introduction

Bound states in the continuum (BICs) are unconventional states, which, despite lying within the radiative continuum band, are completely confined and therefore do not radiate to free space. Historically, the existence of BICs has been first mathematically predicted by Wigner and Neumann in 1929 as the solution of the Schrödinger equation with the potential energy oscillating with asymptotically decreasing amplitude as moving away from the quantum-well[1]. In 1976, Herrick[2] and Stillinger[3] reported BICs in semiconductor superlattice supported by other forms of potentials that was later experimentally observed by Capasso et al. in 1992[4]. After that, the explanation for BIC was not only restricted to only quantum mechanics but also extended to wave physics such as acoustics and hydrodynamics[5,6]. In the wave context, the formation of BIC was described as the destructive interference of radiative waves. In 2008, the concept of BIC has been applied to photonic systems[7,8], and the experimental demonstration was reported in 2011 on an optical waveguide array structure[9] and in 2013 on photonic crystals[10]. The fast development of solid-state platforms, such as two-dimensional materials[11–13], piezoelectric materials[14], Weyl semimetals[15] and topological insulators[16–19], and the physics of metasurfaces, flat optics has offered new platforms for BIC resonances. In 2017, the realization of lasing action

Received: 29 August 2025

Accepted: 26 January 2026

Published online: 16 March 2026

[1]Institute of Materials Research and Engineering (IMRE), Agency for Science, Technology and Research (A*STAR), 2 Fusionopolis Way, Innovis #08-03, Singapore 138634, Singapore; [2]Centre for OptoElectronics and Biophotonics (COEB), School of Electrical and Electronic Engineering, Nanyang Technological University, Singapore 639798, Singapore; [3]CNRS-International-NTU-Thales Research Alliance (CINTRA), IRL 3288, Singapore 637553, Singapore.

†These authors contributed equally to this work.

*Correspondence: JH Teng, E-mail: jh-teng@imre.a-star.edu.sg; ST Ha, E-mail: ha_son_tung@imre.a-star.edu.sg

from BICs in semiconductor membranes[20] has triggered tremendous interests in exploring potentials of BICs in various applications such as nano-lasers, refractometric sensors, nonlinear optics, beam steering and imaging[21–26]. BICs can be supported by two-dimensional periodic arrays, linear periodic chains of resonators and even single subwavelength particles[27].

Due to the non-radiating nature, BIC modes have zero linewidth and do not decay. Quality factors (Q-factors) which describe the energy loss rate of optical resonances, are defined by resonance wavelengths over linewidths. Therefore, theoretically, the radiative Q-factor goes to infinite in the BIC conditions. In practice, the total Q-factor is limited by inevitable lossy channels induced by the finite sample size, the fabrication imperfection, the diffraction into high-index substrates and non-radiative losses including the material absorption. Metallic plasmonic nanostructures, despite being known to be lossy, demonstrated BIC resonances with Q-factor of ~100–300[28] that is improved to ~2500 in hybrid systems combining plasmonic and dielectric materials[29]. However, so far, a fundamental approach to minimize absorption losses and diffraction leaking is using low-loss and high-refractive-index all-dielectrics. A library of all-dielectric nanostructures supporting BICs in different ranges of the electromagnetic spectrum is summarized in Table 1. The Q-factor of all-dielectric resonators can reach 10^6 near the BIC conditions[10].

Due to the dark nature, true BIC modes cannot be optically excited or detected at far field. Therefore, leaky channels are normally created by breaking the structural symmetry to turn a true BIC into quasi-BIC, which has sharp Fano-resonance shape. In photonic metasurfaces, the radiative loss can be controlled by the array size and the structural asymmetric parameters. Overvig et al. has developed a detailed analysis on in-plane perturbations on high-symmetry two-dimensional photonic crystal lattices and selection rules of quasi-BICs based on group theory. It serves as a catalog for design for multifunctional devices with control to spatially control resonant wavefronts[30].

BICs can be classified into symmetry-protected BICs, which decouples to the continuous spectrum due to the symmetry-mismatch and hence located at high-symmetry points of the Brillouin zone (BZ), accidental BICs, which are formed due to time-reversal symmetry and inversion symmetry, Friedrich-Wingent BICs (FW-BICs), which arises from the destructive interference between leaky modes and can be formed at arbitrary points in BZ, and Fabry-Perot BICs (FP-BICs), which is caused by the destructive interference between two distanced resonant cavities. Differently from previous excellent reviews on the applications of BICs[21–26], our review will specifically discuss the fundamental physics underlying different types of BICs, and delve into the recent progress on the design capability, from the conventional approaches of using iterative methods, to the novel inverse design approach based on machine learning which have greatly accelerated the design time and computational resources. In addition to major breakthroughs in super-BICs and chiral BICs, we discuss intriguing concepts of flatband BICs and Moiré BICs, along with exotic phenomena, such as strong light-matter interaction, ultrafast dynamics and exceptional points. We also review the recent advancements and key challenges in BIC-enabled applications. Finally, we offer our perspectives on the promising future of BIC in fundamental research emphasizing on emerging directions such as multilayer metasurfaces, interfacing BICs with quantum emitters, new capabilities enabled by advanced fabrication and design, and pathways towards scalable integration into photonic BIC metadevices. An overview of our paper is summarized in Fig. 1.

2 BIC cavity design

2.1 Physical models and conventional design approach

Figure 2(a) shows the band diagram of the transverse magnetic (TM) mode of a photonic crystal slab. The light line serves as the boundary between different photonics modes: guided modes and leaky modes. Guided modes are situated below the light line and exhibit no radiation into free space due to index guiding effects. In contrast, leaky modes reside above the light line and can radiatively couple with the surrounding medium because of their smaller in-plane wavevector. The leaky modes possess a finite Q-factor due to energy exchange with free space. However, at specific wavevectors (k-points), BIC modes are strictly confined within the photonic crystal slab despite having access to radiation channels.

Fundamentally, a photonic crystal can be understood as a structure possessing translation, rotation and reflection symmetries in both real and reciprocal space. Analyzing these symmetries provides a foundational understanding of the photonic properties. The simplest form of BIC occurs at high symmetry points, where there is a mismatch between the symmetry of the eigenmode and the available radiation channels. Figure 2(b) shows the symmetry operations of C_{4v}-symmetry lattice. This symmetry group $\{E, C_4, C_4^{-1}, C_2, \sigma_x, \sigma_y, \sigma_d^{'}, \sigma_d^{''}\}$ includes the identity (E), 90° rotations (C_4, C_4^{-1}), 180° rotation (C_2), and mirror symmetries about the x, y and diagonal axes ($\sigma_x, \sigma_y, \sigma_d^{'}, \sigma_d^{''}$). At the Γ-point, the optical modes possess the full C_{4v} symmetries. One particularly useful symmetry for identifying BIC states is C_2-symmetry. If $\boldsymbol{E}$ is an eigenmode, $C_2\boldsymbol{E}$ is also an eigenmode differed by a constant: $C_2\boldsymbol{E} = \alpha\boldsymbol{E}(\boldsymbol{r})$. We have $\alpha = \pm 1$ as applying 180° rotation twice inverts the modes back to its original state[82]. Modes can thus be classified as even or odd with respect to C_2 symmetry. Below the diffraction limit, the only radiation channel is the plane-wave represented by $\boldsymbol{E} = E_x\hat{x}e^{-jkz} + E_y\hat{y}e^{-jkz}$, which is odd under C_2 transform. Therefore, any even modes under C_2-transformation are

Table 1 | Summary of all-dielectric materials for the fabrication of BIC resonances at different wavelength ranges.

Range	Material	Bandgap @RT (λ_g nm)	Optical constants[31]	Applications
Deep ultraviolet to ultraviolet	GaN	363	n ~ 2.7 @ 376 nm k ~ 0.2 @ 376 nm	Lasing (λ_{BIC} ~ 376 nm)[32]
	Diamond	227	n ~ 2.5 @ 300 nm k ~ 0 @ 300 nm	Biosensing (λ_{BIC} ~ 240–340 nm)[33]
	PEA_2PbBr_4(*)	365 (@5 K)	n ~ 2.5 @ 416 nm k ~ 0.1 @ 416 nm	UV resonator (λ_{BIC} ~ 416 nm)[34]
Visible	TiO_2	387 nm	n ~ 2.6 @ 630 nm	Lasing (λ_{BIC} ~ 630 nm)[35,36]
	HfO_2	221 nm	n ~ 1.9 @ 426 nm	Visible resonator (λ_{BIC} ~ 426–673 nm)[37]
	hBN	194 nm	n ~ 2.1 @ 426 nm	SHG (λ_{BIC} ~ 400–975 nm)[38]
	Transition metal dichalcogenides	620 nm	n_{WS_2} ~ 4.2 @ 585 nm	Exciton polaritons (λ_{BIC} ~ 585 nm[39], λ_{BIC} ~ 600–800 nm[40,41]
	InGaP	625 nm	n ~ 3.5 @ 625 nm k ~ 0 @ 625 nm	Lasing (λ_{BIC} ~ 650 nm)[42]
	Si_3N_4	234 nm	n ~ 2.0 @ 532 nm	Sensing: λ_{BIC} ~ 530 nm[43,44]; λ_{BIC} ~ 780 nm[45] Imaging: λ_{BIC} ~ 530 nm[46]
	Si	1107 nm (indirect)	n ~ 3.8 @ 700 nm k ~ 0 @ 700 nm	Sensing: λ_{BIC} ~ 650–770 nm[47]
	PEA_2PbI_4	530 nm	n_∞ ~ 2.4	Exciton polariton: λ_{BIC} ~ 490–530 nm[48,49]
Near- infrared to Mid-infrared	Si	1107 nm (indirect)	n ~ 3.7 @ >826 nm k ~ 0 @ >826 nm	Sensing: λ_{BIC} ~ 850 nm[50]; λ_{BIC} ~ 1400 nm[51]; λ_{BIC} ~ 1550 nm[52,53]; λ_{BIC} ~ 737–1017 nm[54]; λ_{BIC} ~ 6667 nm[55] SHG (λ_{BIC} ~ 1550 nm)[56] THG (λ_{BIC} ~ 1400 nm)[57,58] HHG (λ_{BIC} ~ 3978 nm)[59] Chiroptical response with CD~0.93 and THG (λ_{BIC} ~ 1400 nm)[60] Both SHG and THG (λ_{BIC} ~ 1500 nm)[61] Polarization-independent THG and FHG (λ_{BIC} ~ 1550 nm)[62]
	GaP	553 nm	n ~ 3.2 @ 800 nm	SHG (λ_{BIC} ~ 1200 nm)[63] SFG (λ_{BIC} ~ 1545 nm)[64]
	GaAs	873 nm	n ~ 3.5 @ 800 nm	Lasing (λ_{BIC} ~ 825 nm)[65,66] Integrating quantum dots on Si-devices (λ_{BIC} ~ 1270 nm)[67] Polariton condensation (λ_{BIC} ~ 816 nm)[68]
	$Al_{0.2}Ga_{0.8}As$	742 nm	n ~ 3.3 @ >800 nm k ~ 0 @ >800 nm	SHG (λ_{BIC} ~ 1550 nm)[69]
	$In_xGa_{1-x}As_yP_{1-y}$	1345 nm	n ~ 3.1–3.5 @ 1550 nm	Lasing (λ_{BIC} ~ 1558 nm)[20,70]
	As_2S_3	539 nm	n ~ 2.5 @ 1000 nm	THG (λ_{BIC} ~ 900–1200 nm)[71]
	Ge	1550 nm (indirect)	n ~ 4.7 @ 827 nm k ~ 0.3 @ 827 nm	Sensing (λ_{BIC} ~ 7142 nm)[72] Phonon polaritons (λ_{BIC} ~ 5600 nm)[73]
	$Ge_{1-x}Sn_x$(*)		n ~ 4.2 @ 1250 nm [74]	Ultrahigh-Q cavity (λ_{BIC} ~ 1250 nm)[74]
	$LiNbO_3$	329 nm	n ~ 2.2 @ 1300 nm k ~ 0 @ 1300 nm	SHG (λ_{BIC} ~ 1300 nm)[75]
THz	Ge	1550 nm (indirect)	n ~ 4 @ 0.75 THz[76]	Ultrafast modulator (λ_{BIC} ~ 4×10^5 nm – 0.75 THz)[76]
	Si	1107 nm (indirect)	n ~ 3.45 @ 1 THz[77]	Super-BIC cavity[77] High-Q BIC[78,79]
	GaAs/AlGaAs	~770 nm	n ~ 4.3 @ 3 THz[80]	Lasing[80]
Microwaves	Polymer ceramic composites	--	n ~ 4.6 @ 30 cm	High-Q BIC at microwave wavelength (λ_{BIC} ~ 30 cm)[81]

(*)theory only, RT = room temperature, SHG = second-harmonic generation, THG = third-harmonic generation, FHG = fifth-harmonic generation, HHG = high harmonic generation, SFG = sum-frequency generation, PEA = phenethylammonium.

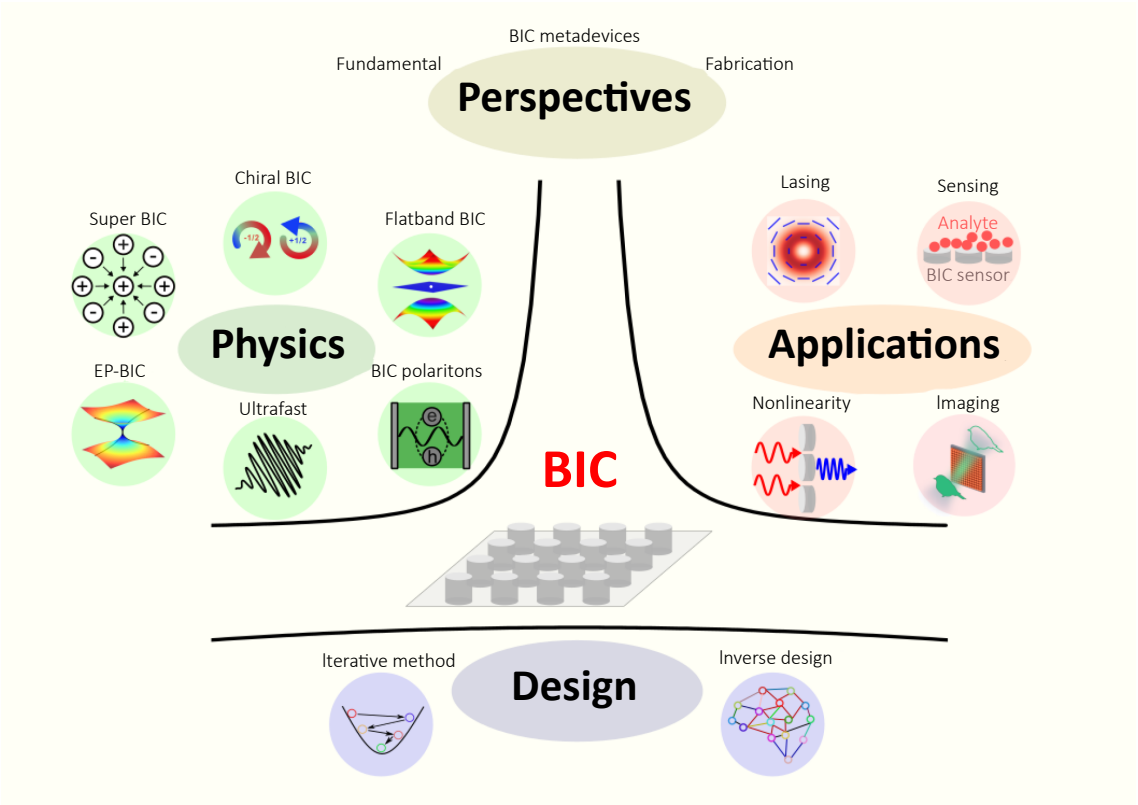


Fig. 1 | Overview of the recent advances in BIC cavities, from design methodologies and physics to applications with prospects in fundamental research, advanced fabrication processes and the development of BIC metadevices.

unable to couple to the radiation and become BIC states.

The concept of symmetry-protected BIC involves a single eigenmode. However, when multiple eigenmodes share the same radiation channel, far-field radiation can be cancelled out due to destructive interference, giving rise to what is known as Friedrich-Wintgen BICs. We consider two resonances with resonance energy E_1, E_2 and radiative rates of γ_1, γ_2. The Hamiltonian of the system can be written as: [86,87]

$$\boldsymbol{H} = \begin{pmatrix} E_1 & \kappa \\ \kappa & E_2 \end{pmatrix} - \mathrm{i}\begin{pmatrix} \gamma_1 & \mathrm{e}^{\mathrm{i}\varphi}\sqrt{\gamma_1\gamma_2} \\ \mathrm{e}^{\mathrm{i}\varphi}\sqrt{\gamma_1\gamma_2} & \gamma_2 \end{pmatrix} , \quad (1)$$

here κ and $\mathrm{e}^{\mathrm{i}\varphi}\sqrt{\gamma_1\gamma_2}$ signifies the near-field and far-field coupling strength, and φ is the phase difference between the two modes. The eigenvalues can be expressed as:

$$E_{\pm} = \frac{E_1+E_2}{2} - \mathrm{i}\frac{\gamma_1+\gamma_2}{2} \pm \sqrt{\left(\frac{E_1-E_2}{2} - \mathrm{i}\frac{\gamma_1-\gamma_2}{2}\right)^2 + \left(\kappa - \mathrm{i}\mathrm{e}^{\mathrm{i}\varphi}\sqrt{\gamma_1\gamma_2}\right)^2} . \quad (2)$$

Applying the following condition derived by Friedrich-Wintgen[88]:

$$(E_1 - E_2)\cdot p\sqrt{\gamma_1\gamma_2} = \kappa(\gamma_1 - \gamma_2) , \quad (3)$$

where p represents the parity difference of the modes.

The eigenvalues become:

$$E_+ = \frac{E_1+E_2}{2} + p\frac{\kappa}{\sqrt{\gamma_1\gamma_2}}\cdot\frac{\gamma_1+\gamma_2}{2} - \mathrm{i}(\gamma_1+\gamma_2) , \quad (4)$$

$$E_- = \frac{E_1+E_2}{2} - p\frac{\kappa}{\sqrt{\gamma_1\gamma_2}}\cdot\frac{\gamma_1+\gamma_2}{2} , \quad (5)$$

here, E_- become purely real, indicating a BIC with no radiative loss. In contrast, the damping rate of E_+ becomes $(\gamma_1+\gamma_2)$, indicating a higher radiative loss. This can be understood as the destructive and constructive interference of the two resonances. Such BICs are often found at the avoided crossing of two bands and typically require fine-tuning of system parameters[89].

Fine-tuning the geometrical parameters can lead to another type of BIC at generic wavevectors (k-points)[10]. These so-called accidental BICs involve only one mode and not protected by symmetry that are distinct from the symmetry-protected and FW-BIC. Their existence can be attributed to the combined effects of time-reversal symmetry and inversion symmetry. In an infinite photonic slab, the field distribution of eigenmodes is described by the Bloch theorem:[10,82,90] $\boldsymbol{E} = \mathrm{e}^{\mathrm{i}\boldsymbol{k}\rho}\boldsymbol{u}_{\boldsymbol{k}}(\rho, z)$, where $\boldsymbol{E}$ is the electric field, $\boldsymbol{k} = k_x\hat{\boldsymbol{x}} + k_y\hat{\boldsymbol{y}}$ is the in plane wavevector, $\rho = x\hat{\boldsymbol{x}} + y\hat{\boldsymbol{y}}$ is the in-plane coordinates and $\boldsymbol{u}_{\boldsymbol{k}}$ is a periodic function in the x−y plane. Below the diffraction limit, the only outgoing wave is the zeroth order diffraction mode, with Fourier coefficients

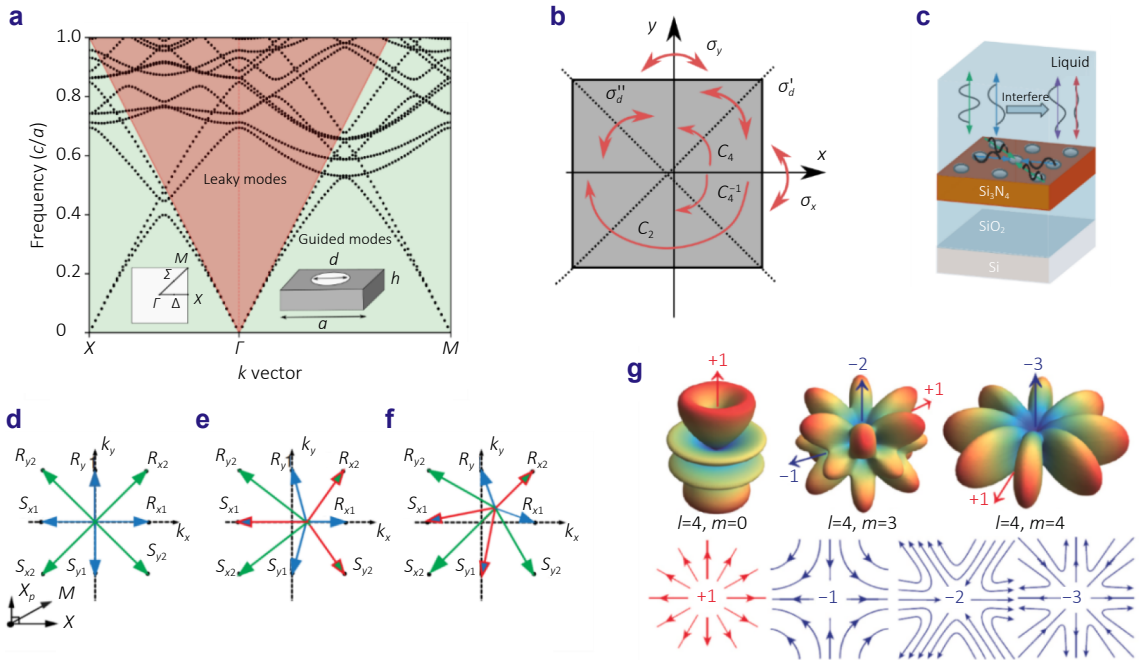


Fig. 2 | (a) The band diagram of a photonic slab consisting of Si_3N_4 film with air holes. The light line divides the mode into guided modes and leaky modes. The insets show the unit cell parameters and the first Brillouin zone of the reciprocal space lattice. (b) Symmetry operations of a C_{4v} lattice. (c) Schematic of a Si_3N_4 photonic crystal on a silica cladding layer on top of a silicon substrate. The top liquid layer is the refractive-index matching layer to ensure the vertical symmetry ($n_{liquid} = n_{SiO_2}$). The phase matching condition for (d) *G*-point, (e) k = 0.25 μm^{-1} along the *Γ*-*X* direction; (f) $k = \sqrt{2}/6$ μm^{-1} in the *Γ*-*M* direction. Arrows with the same color indicate wave vectors from equivalent high symmetry points. (g) Top: radiation pattern of a few selected multipoles with arrows pointing to the null intensity. Bottom: The polarization pattern for singular points with different topological charges. Figure reproduced with permission from: (c–f) ref.[83], American Physical Society; (g) ref.[85], American Physical Society.

for s and p polarizations expressed as[10]: $c_s(\boldsymbol{k}) = \langle \widehat{\boldsymbol{e}}_{\boldsymbol{k}} \cdot \boldsymbol{u}_{\boldsymbol{k}} \rangle$, $c_p(\boldsymbol{k}) = \langle \widehat{\boldsymbol{e}}_{\boldsymbol{k}} \cdot \boldsymbol{v}_{\boldsymbol{k}} \rangle$, where $\boldsymbol{u}_{\boldsymbol{k}}, \boldsymbol{v}_{\boldsymbol{k}}$ are the electric and magnetic periodic function at a distance away from the photonic slab, and $\widehat{\boldsymbol{e}}_{\boldsymbol{k}} = (k_y, -k_x, 0)/|\boldsymbol{k}|$. The angle brackets denote integration over one unit cell. The combined time-reversal symmetry and inversion symmetry, $\varepsilon(x, y, z) = \varepsilon^*(-x, -y, -z)$, allows c_s, c_p to be either real or imagery simultaneously[10,90]. This reduced the total degree of freedom and thus the condition: $c_s, c_p = 0$ can be met with parameter tuning. In some systems, this can be achieved by simply varying the k_x and k_y, giving rise to accidental BICs at generic k-points. This argument also suggests that a BIC point is a singular point where the nodal lines of $c_s = 0$ and $c_p = 0$ meet, illustrating the role of BIC as a topological polarization singularity[90].

The concepts of symmetry-protected and accidental BIC can also be explained by decomposing the outgoing wave into plane-wave basis using Bloch theorem. The destructive interference of these guided modes through the in-plane closed channel and the out-of-plane radiative channel[83]. This is conceptually shown in Fig. 2(c). Using Fourier expansion, the Bloch theorem can be further written as[91]: $\boldsymbol{E} = \sum_{\boldsymbol{G}_{mn}} c_{mn} e^{-j(\boldsymbol{k}+\boldsymbol{G}_{mn})\rho}$, where c_{mn} are the Fourier coefficients and $\boldsymbol{G}_{mn} = m\boldsymbol{b}_1 + n\boldsymbol{b}_2$ with $\boldsymbol{b}_1$ and $\boldsymbol{b}_2$ being the reciprocal lattice vectors. As shown in Fig. 2(d–f), each Fourier coefficients contributes to the radiation with different phases and intensities. The symmetric nature of these wavevectors results in destructive interference at any arbitrary k-points.

Apart from the plane-wave basis, the outgoing wave of a photonic crystal slab can also be decomposed to a series of vector spherical harmonics as following[92,93]: $\boldsymbol{E}(\boldsymbol{r}) = \sum_{j=1}^{\infty} \sum_{m=-j}^{m=j} [a_{jm}\boldsymbol{N}_{jm}(\boldsymbol{r}) + b_{jm}\boldsymbol{M}_{jm}(\boldsymbol{r})]$, where $\boldsymbol{N}_{jm}(\boldsymbol{r})$ and $\boldsymbol{M}_{jm}(\boldsymbol{r})$ are the electric and magnetic multipolar vector fields and a_{jm} and b_{jm} are the corresponding expansion coeffecients. Intrinsically, these electric and magnetic multipoles have nodes with zero radiation in highly symmetric directions, corresponding to symmetry-protected BICs[94]. The combination of multiple multipole components also leads to the cancellation of radiation in certain directions, which explains the off-*Γ* BICs[94]. Furthermore, different multipolar patterns exhibit distinct vector characteristics in the far field, contributing to the understanding of the vectorial singularity nature of BICs[84]. Figure 2(g) illustrates examples of these multipolar patterns, showcasing their unique polarization topology and nodes of zero intensity.

Understanding the mechanisms behind different types of BICs provides valuable insight into designing BICs at specific wavelengths and k-points. The most common approach to achieve BIC design involves sweeping the geometries, for example finite-difference time-domain (FDTD), finite element method (FEM), guided-mode

expansion, rigorous coupled-wave analysis (RCWA), which require iterative search and sweeping parameters in multidimensional space and hence, computationally expensive and time-consuming. Furthermore, the potential of these methods is limited to relatively simple geometry. For symmetry-protected BICs, tuning the geometry shifts the BIC wavelength while keeping the k-point fixed[95]. Thus, only a single tuning parameter is typically needed to achieve BIC at a specific wavelength. In contrast, for accidental BICs and FW BICs, modifying a single geometrical parameter leads to shifts in both the wavelength and k-point. Therefore, multiple tuning parameters, such as the lattice size, geometrical shapes, and the thickness of the photonic crystal, are generally required to achieve the desired BICs[70,96].

2.2 Machine learning and inverse design approach

Although the topological properties and high quality factor of a simple isolated BIC, have enabled a plethora of new applications, recent advances in this field have brought exciting development in combining BIC with other unique photomesons, such as introducing BIC to zeros index materials[97,98], controlling the interaction of multiple BIC[70,99,100], tuning the chirality and polarization properties of BIC[101,102], controlling the topological charge[103]. Conventional methods based on analytical models and parameter sweeping become increasingly challenging for these complex functionalities because they require tuning multiple and intercoupled parameters in both real space and k-space. Inverse design algorithms[104–108] are powerful tools to tackle this challenge. Not only can they be applied to explore large numbers of design parameters but also generate designs with freeform geometries that cannot be defined by simple geometrical parameters. For example, zero-index BIC is achieved by complex shapes described by a Fourier series of the polar coordinates[97]. Tuning of multiple BICs is achieved by freeform geometries represented by a latent vector interpretable by neural networks[109].

The starting point of an inverse problem is typically the desired optical response and an optimization method is used to find a design that matches the desired response as close as possible. Inverse design methods can be divided into two categories: conventional iterative methods and data-driven methods. In conventional methods, a figure of merit (FOM) function represents how close the current optical response is to the desired one. The FOM function is improved iteratively by optimization algorithms such as gradient descent, particle swarm optimization, simulated annealing and so on. The algorithm terminates when the FOM cannot be improved further. Data-driven methods use pre-obtained data to train various machine learning frameworks to capture the statistical distribution of these data and to generalize to new designs not far away from the initial training data set. Both the iterative methods and the data-driven methods are well-reviewed and interested readers can refer to these works[104–108]. Here, we focus on the inverse problem in BIC design, which poses unique challenges for the inverse design algorithm.

For the gradient descendent algorithm, the challenge is to calculate the derivative of the FOM functions with respect to the input parameters accurately and efficiently. One solution is the adjoint method. It is well suited for a general linear scattering problem with the form $\boldsymbol{Ae} = \boldsymbol{b}$, where $\boldsymbol{A}$ is the representation of the system under study, $\boldsymbol{e}$ is the field distribution and $\boldsymbol{b}$ is the source[110]. The gradient FOM can be expressed as a function of the forward field and adjoint field due to the Lorentz reciprocity[107]. Minkov et al.[110] expanded this method to the eigenvalue problem by using automatic differentiation, which formulates the eigenvalue problem into a computation graph that traces the gradient of all the fundamental operations and calculates the overall gradient by the chain rule. Using this method, they came up with a complicated photonic slab design that features a Dirac cone formed by the accidental degeneracy of 3 symmetry-protected BIC at the G-point. The Dirac cone dispersion allows the structure to maintain a high Q-factor with zero effective indexes.

Compared to iterative methods, machine learning algorithms can boost the inverse design speed. At a one-time training cost, the algorithm can be used for on-demand inverse design. A challenge for machine learning algorithms is the representation of BIC modes. Since BIC emerges as vanishing linewidth in the reflection and transmission spectra, they take up only a few data points, if any, in the whole reflection or transmission spectrum. They are easily overshadowed by broader background peaks because the broader peaks have more statistical significance. This could lead to the failure of the machine learning algorithm. A solution is to decompose the spectrum into an analytical sum of Fano, Lorentzian, and Gaussian peaks and to establish the mapping between these analytical parameters with the geometrical parameters[111,112]. However this means the design only works for quasi-BIC with spectral features. Another strategy is to solve the eigenmodes and pick out the BIC based on the Q-factor or the symmetry of the modes[109,113,114]. The limitation of this method is that the transmission and reflection spectra excited with a broadband light source cannot be predicted directly. We envision that these conflicting challenges can be addressed through more advanced design strategies, such as integrating eigenmode analysis with spectral optimization during inverse design. Another promising direction is the use of physics-informed machine learning algorithms, which embed the underlying physics of optical resonances directly into the network architecture. Although such methods have already been applied to BIC design, their current implementations remain largely constrained to quasi-BIC regimes[109,111,113–118].

Table 2 summarizes recent advances in design algorithms for BICs. Achieving high-performance designs with minimal datasets remains a central objective, and several

Table 2 | Summary of recent advances in design algorithms for BICs.

Dataset size/ iterations	Training strategy	Type	Figure of merit (FoM)
26881 (ref.[115])	Transformer forward neural network plus inverse neural network	quasi-BIC	Prediction efficiency increased by 96.5% compared to multilayer perceptron model
68 (ref.[117])	Prior knowledge-guided generative diffusion model	quasi-BIC	Improvements exceeding 30% in key resonance metrics over classical designs
29400 (ref.[116])	Multi-head self-attention-based transformer	quasi-BIC	99% prediction error reduction compared to conventional transformer model
17161 (ref.[118])	Transfer learning with fully connected neural networks	quasi-BIC	Network error <1.2%, and the FoM prediction error <2%, effective sensing area prediction error <0.5%
~4000 (ref.[111])	Physics informed transfer learning based on convolutional neural network	quasi-BIC	95% prediction accuracy
50000 (ref.[113])	Physics-inspired inverse design with neural network	BIC	1% error with desired BIC
3000–6000 (ref.[119])	Fully connected neural networks with sparse identification of nonlinear dynamics	quasi-BIC	R^2~0.627, RMSE~0.14, MAE~0.109
1100 (ref.[120])	Random parameter adjustment process combined with a convolutional neural network	Mini-BIC	$Q \sim 6.32 \times 10^5$ ($Q \sim 4.32 \times 10^4$ in the baseline design)
18000 (ref.[109])	Generative model	BIC	BIC wavelength accuracy ~ ±15 nm
121 (ref.[121])	Random forest	EIT	The simulation time is reduced from 3 months to one-hour
~10000 (ref.[122])	Random forest	quasi-BIC	R^2>0.7
NA (ref.[123])	Random forest	quasi-BIC	$Q > 10^4$
550 iterations (ref.[124])	Adjoint-based gradient driven optimization	quasi-BIC	$Q \sim 6 \times 10^6$
100–400 iterations (ref.[125])	Adjoint-based topology optimization	quasi-BIC	$Q \sim 435$, CD ~ −0.76

(EIT = electrically induced transparency, RMSE = root mean squared error, MAE = mean absolute error, CD = chiral dichroism)

encouraging developments have emerged. For example, physics-informed machine learning techniques can reduce the required dataset to fewer than 100 samples[117]. It is also encouraging to see machine learning and other inverse-design approaches leveraging BIC physics have enabled the realization of a variety of novel, high-performance optical metasurfaces. Despite some exciting progress, the potential of the inverse design algorithms in the BIC design is still yet to be fully uncovered. We expect further developments to be made in aspects such as on-demand BICs at specific k-point and wavelength, complex polarization control, complex topological control, arbitrary manipulation of multiple BIC points and the novel physics based on these complex geometries.

3 Manipulation of BICs and novel physics

3.1 Manipulation of BIC topological charges

3.1.1 Topological charges

The game-changing discovery on BICs is their topological nature[90] that has opened new opportunities for tailoring photonic structures to add new functionalities for various advanced research and applications. The description of BIC topological charges is analogous to Pancharatnam-Berry phase topology, which correlates the orientations of polarizations and the spin of incident photons. Due to the topological nature, photons associated with BIC mode possess a vortex characteristics[126]. Therefore, understanding the charges of BIC in photonic systems allow us to design vector beams and their spin properties. Furthermore, it leads to exotic physics such as spin-Hall effect of light, in which left-handed and right-handed polarized photons are deflected along different directions[127]. Abdrabou et al. generalized a theory for the minimum number of tunable parameters to preserve a nondegenerate BIC for specified structural perturbations[128].

BICs in periodic photonic lattices manifest themselves as singularities of polarization vortices in the far-field radiation, where BICs appear at the vortex center[129,130]. The polarization states include linear polarization, elliptical polarization and circular polarization. A vortex is characterized by its topological charge, which is defined as the winding number of the polarization vector around the singularity:

$$q = \frac{1}{2\pi} \oint_C \mathrm{d}\boldsymbol{k} \cdot \nabla_{\boldsymbol{k}} \rho(\boldsymbol{k}), \tag{6}$$

where $\rho(\boldsymbol{k}) = \arg[c_x(\boldsymbol{k}) + \mathrm{i}c_y(\boldsymbol{k})]$ is the angle of the polarization vector projected on x-y plane as a function of wavevector $\boldsymbol{k}$, $\boldsymbol{c}(\boldsymbol{k}) = c_x(\boldsymbol{k})\hat{\boldsymbol{x}} + c_y(\boldsymbol{k})\hat{\boldsymbol{y}}$ is the polarization vector, and C is a closed path going around the vortex in the anticlockwise direction. The topological charges strongly depend on the point-group symmetries of metasurfaces[90],

which suggests that BICs can freely move in k-space, while structural parameters are varied as long as the system symmetries are kept unaltered.

3.1.2 Manipulation of topological charges for advanced functionalities of BIC cavities

The charges can be generated or annihilated by modifying the structural parameters such as slab thickness and period, while the total charge is conserved[131,132]. The charge conservation allows us to predict the behavior of the systems upon major parameter changes. For example, when several BICs with total charges zero collide, the BIC disappears. A BIC with integer charge can also decay into several BICs with half-integer charges that exhibit circular polarization. The topological physics of BICs has been further extended to a new concept of bound topological edge states in the continuum introduced by Zhang et al.[133]. The authors proposed a scheme combining topological bandgap and BIC at the air edges of nontrivial photonic crystals. Two bound topological edge states with divergent Q-factor and different inherent helicities are generated that can merge by changing the radius of the defect cylinders.

3.2 Super BICs

In various applications, high-Q resonators with strong field enhancement and amplified optical signals are required for low-power consumption. In this regard, BICs are advantageous because of the suppressed cavity losses and high tolerance to fabrication imperfections owing to their topologically protected nature. However, a main drawback of BICs is the fast decay of their Q-factor decays as moving away from the singularity in the reciprocal space, i.e. $Q_{\mathrm{BIC}} \sim 1/(k-k_{\mathrm{BIC}})^{2|q|}$ that introduces scattering loss channels and limits the device performance[99]. In most cases, the Q-factor reduces to $Q_{\mathrm{BIC}} \sim 1/(k-k_{\mathrm{BIC}})^{2}$ for the charge +1 or −1. A viable route is merging multiple BICs in reciprocal space to form a super-BIC state. Topological charges, defined by the polarization vector projected on the (x,y)-plane, requires $c_x(\boldsymbol{k})$ and $c_y(\boldsymbol{k})$ to be real that is protected by the rotational symmetry about z-axis, time-reversal symmetry and σ_h (up-down mirror symmetry in z-direction) of photonic systems. BICs are allowed to move along the symmetric directions. Therefore, by breaking the appropriate symmetry via tuning structural parameters, BICs can be controlled in reciprocal space. Four main merging mechanisms can be categorized as: (i) merging multiple FW-BICs or accidental BICs with a symmetry-protect BIC pinned at Γ-point, (ii) merging FW-BICs with accidental BICs at off-Γ-point, (iii) merging the split BICs from a high-order BIC with accidental BICs at off-Γ-point and (iv) merging extrinsic BICs from an external cavity with intrinsic BICs. Depending on the design objectives, specific symmetries and structural parameters are selectively broken to control individual BICs accordingly. While (i) and (ii) can be achieved by changing symmetry-independent parameters such as thickness of the photonic crystal slab or periodicity, (iii) require breaking the structure symmetry from, for example, C_6^z or C_3^z to C_2^z. Finally, the mechanism (iv) enriches the design possibility to construct super-BIC configurations by introducing an additional degree of freedom for BICs manipulation. The topological scaling rule of the $Q_{\text{super-BIC}}$ depends on the involved topological charges, the types of BICs and the merging mechanisms.

In a pioneering work, Jin et al.[99] has designed a photonic crystal (PhC) slab with a square lattice of circular air holes that supports 9 BICs in the TE A band (Fig. 3(a)). The distribution of the BICs in the momentum space is shown in Fig. 3(b) for different scenarios. When the periodicity $a = 519.25$ nm, the 9 BICs are far apart, including a symmetry-protected BIC pinned at Γ-point, and 8 accidental BICs located at off-Γ-point. Each BIC carries a topological charge of +1 or −1 that is represented by a polarization vortex as shown in Fig. 3(b), bottom panel. By changing the sample periodicity a, the accidental BICs move in k-space towards the center. When the periodicity hits a critical value $a_c = 531.42$ nm, all the 9 BICs merge into a single isolated BIC (Fig. 3(b)). The Q-factor diverges at $k = 0$, and the divergence of the Q-factor reduces to $Q_{\text{super-BIC}} \sim 1/k^6$, leading to 12-time enhancement of Q at nearby states compared with the single-BIC design (Fig. 3(c)). When a is off from a_c, Q-factor returns to $Q \sim 1/k^2$. By using the super-BIC concept, a record low lasing threshold of 1.47 kW/cm^2 has been achieved with Q-factor of up to ∼7300[70]. This threshold is 50 to ten millions times smaller than previously reported BIC lasers[20,65,134,135].

Merged BICs can be achieved at not only at Γ-point ($k = 0$) but also at any oblique angles ($k \neq 0$) by breaking proper symmetries[77,131,136] that extends the applications of supercavities in beam steering, directional emissions, modulators and sensors, in which the angular selectivity is required. Kang et al. demonstrated the merging of a FW-BIC and an accidental BIC in a square array of circular air holes on a Si_3N_4 PhC (Fig. 3(d)). By varying the thickness of photonic crystal slabs (Fig. 3(e)), the coupling between photonic modes is altered that brings the FW-BIC and the accidental BIC close to each other. The Q-factor of the merged BIC is enhanced to $\sim k^{-4}$ [136]. The merged BIC is no longer restricted at only high symmetry points but can be continuously tuned in k-space by further breaking proper symmetries. For example, when the circular air holes are modified into elliptical shape, all the in-plane mirror symmetries are broken while C_2^zT symmetry is preserved. By varying the thickness, the accidental BICs can merge at any arbitrary $\boldsymbol{k}$-point[136]. The scaling rule of Q-factor can be noticeably tailored to $Q_{\text{super-BIC}} \propto k^{-8}$ by merging multiple fundamental BICs with a higher-order BIC with $|q| = 2$, which is supported by high symmetry groups or higher

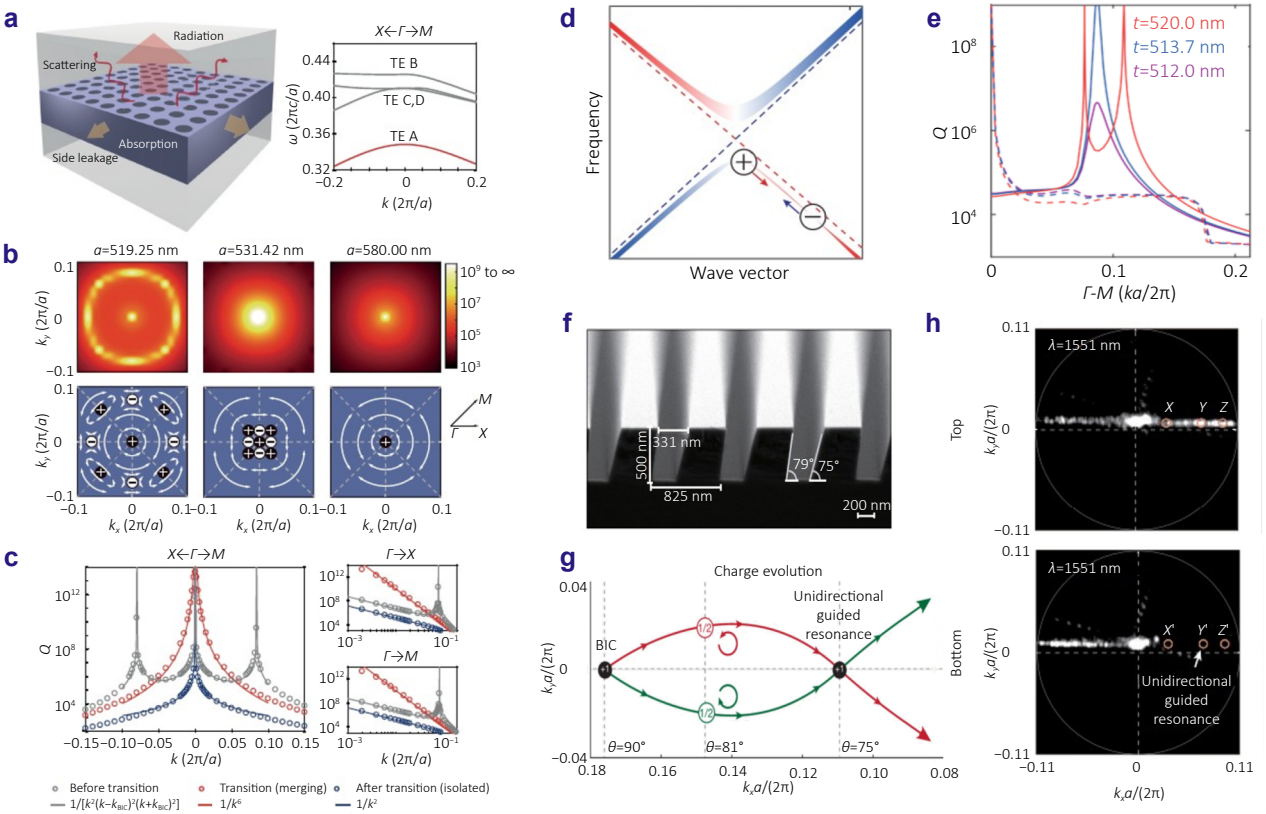


Fig. 3 | (a) Schematic of the photonic crystal design with the loss channels and the calculated band structure. (b) Several BIC modes appear on the band TE A, where the *Q*-factor is simulated (top) and the polarization plot at far-field for different periodicity *a*, where nine BICs with the total charge +1 merge into a single BIC (bottom). (c) Simulated *Q*-factor for BIC modes before and after merging as a function of *k*. (d) Merging of FW BIC and accidental BIC as structural parameter varies. (e) Distribution of *Q*-factor along *G*-*M* direction for different sample thicknesses. (g) Trajectories of the two half-integer charges in *k*-space when the tilting angle varies. (h) Intensity of the upward (top) and downward (bottom) radiation showing the suppressed signal of the downward signal at UGRs. Figure reproduced with permission from: (a–c) ref.[99], Springer Nature; (d, e) ref.[136], American Physical Society; (f–h) ref.[100], Springer Nature.

energy bands. The Q enhancement of the nearby states can be generalized to $Q_{\text{super-BIC}} \propto k^{-2|q|-4}$ [77,103]. Interestingly, by reducing the system symmetry from C_6^z to C_2^z (e.g., elliptical air holes, deformed lattice), high-order topological charges (e.g., $|q| = 2$) at high-symmetric points (Γ-point) can split into few low-order charges (e.g., $|q| = 1$) at off-Γ-point[103,131], which can merge with accidental BICs or FW-BICs to form super-BICs at any point in the reciprocal space.

By considering 5 BICs originated from all 3 different types (i.e., symmetry-protected BICs, FW-BICs and accidental BICs), Liu et al. theoretically proved the scaling rule $Q_{\text{super-BIC}} \sim k^{-10}$ [137]. In order to further improve the Q-factor, a hybrid system, consisting of extrinsic Fabry-Perot BICs originating from a multilayer structure and three intrinsic BICs in an 1D photonic crystals, unlock another symmetry-independent parameter to manipulate BICs. By tuning the gap distance between the PhC and Fabry-Perot cavity, 5 intrinsic BICs of the three types and two extrinsic BICs merged. As a result, the system can acquire significantly enhanced $Q_{\text{super-BIC}} \sim k^{-14}$ for merging at Γ-point and $Q_{\text{super-BIC}} \sim k^{-6}$ for merging at off-Γ-point [137]. The concept of supercavities utilizing the topological nature of BICs has enabled the engineering of optical resonators for significantly enhanced Q-factors at a broader range of angles. An alternative approach to suppress the scattering loss and attain robustly ultrahigh Q-factor for BIC cavities is by introducing lattice perturbation that converts guided modes into Brillouin-zone and significantly enhances their Q-factors[78,79]. Additionally, emerging half-integer charges in momentum space leads to unidirectional guided resonances (UGRs) mode as reported by Yin et al. for telecommunication regime[100]. While the conventional designs for UGRs using mirrors are bulky, complex, dispersive and dissipative, the idea of using merged BIC modes results in simple, compact and high-efficiency optoelectronic devices. The system consists of an array of 500-nm high silicon grating structure (Fig. 3(f)). When the sidewall is tilted from vertical direction, the two half-integer charges move in the k-plane with the same k_x but opposite k_y. When left-handed and right-handed photons meet, the output photon becomes unidirectional because the radiation cannot exist at both states at the same time (Fig. 3(g)). Figure 3(h) shows the

comparison between the upward (top) and downward (bottom) signal under resonant excitation for the mode at $k_y = 0.01(2\pi/a)$. For the resonances at URGs, the downward radiation is negligible compared with the upward radiation, while for those off from URGs, the upward and downward signals are comparably strong. Not limited to fundamental BICs with $|q| = 1$, Yoda and Notomi demonstrated the deterministic manipulation of high-order charges $q = -2$ into two accidental BICs or into several circularly polarized states by breaking the C_6-symmetry of the system[131].

3.3 Chiral BICs

Chirality describes the property of an object that cannot be superimposed onto its mirror image. Chirality in optical fields arises due to the rotating electric and magnetic field as well as orbital angular momenta creating a helical phase front. The study of the chiral light-matter interactions has practical significance for biological and pharmaceutical applications to boost the detection of chiral enantiomers[138,139], enables novel technologies for communication and optical computing[140,141]. The most widely observed forms are optical rotation (OR) and circular dichroism (CD). OR characterizes the different phase response for left-circularly polarized (LCP) and right-circularly polarized (RCP) light, while CD characterizes the difference in the optical absorption for different handedness. Furthermore, the nanoscale spin-orbit interaction gives rise to a plethora of novel phenomena such as spin-to-vortex conversion and photonic spin-Hall effect[142]. Chiral optical interaction is a very broad topic, which has been discussed in previous comprehensive reviews[143,144]. Here, we focus on some of the latest development related to chiral effects using BICs in dielectric metasurfaces. Indeed, the combination of BIC and chirality has been applied in many fields such as nonlinear vortex generation[145,146,147] sensing and sorting enantiomers[148,149], terahertz applications[150,151] and lasing[102,134].

The study of symmetry-protected BIC shows the integer topological charge of *V*-points splits into pairs of *C*-points with half topological charge (±1/2) and an *L*-line by breaking the in-plane C_2 symmetry (Fig. 4(a)). Different topological configurations such as "lemon", "star" and "monstar" were found for different BICs[152]. Meanwhile, the breaking of integer topological charge into a pair of *C*-points was also observed for off-Γ accidental BICs[153]. The study of a symmetry-protected BIC with a higher topological number (−2) in a C_6 symmetry photonic lattice shows the splitting of the BIC into a more complicated configuration. It can generate not only off-Γ BICs with lower topological charges but also *C*-points with opposite topological charges and the same handedness[131]. This was demonstrated experimentally after that[154]. Subsequently, by reducing the mirror symmetry while keeping the inversion symmetry in the vertical direction, the pair of *C*-points with the same handedness but opposite topological charges can be generated and manipulated with the geometrical parameters (Fig. 4(b)). Two *C*-points with the same half-integer topological charge but different handiness merge into a *V*-point, while *C*-points with the same handiness but opposite topological charges annihilate[132].

Extrinsic chirality can be observed when the incidence angle coincidence with these *C*-points, even if the structure itself is achiral[156]. In contrast, intrinsic chirality refers to the chiral optical effects at a normal incidence. Intrinsic chirality in planar metasurfaces with out-of-plane mirror symmetry is forbidden by symmetry and reciprocity[157]. Therefore, all symmetries must be eliminated to achieve intrinsic chirality. One such design adopts the stacking of two layers of scatterers (Fig. 4(c)). By the rotation of each layer, the eigenpolarization can be arbitrarily elliptical while maintaining high *Q*-factor Fano resonances[155]. An alternative way to break the out-of-plane mirror symmetry is the height differences in the structure. By tuning the height difference and rotational angles of two dielectric bars, the coupling of one handedness can be eliminated while the opposite handedness is critically coupled, resulting in maximum CD[158]. Subsequently, this idea is realized experimentally by a novel multi-step fabrication process[159]. In a lossless medium, a similar method can be used to achieve the total transmission of one helicity and the total reflection of the opposite helicity[160]. Chiral BIC plasmonic metasurface were also demonstrated numerically by taking advantage of the height difference in a 3D structure[161]. Creating height difference is challenging for current nanofabrication techniques. A more practical way to break out-of-plane symmetry is to use slanted geometry (Fig. 4(d)). Experimentally, the slanted side wall is achieved by placing the sample on a wedged substrate and placing an ion collimator above the sample during dry etching. By tuning the incline angle as well as the in-plane geometry, intrinsic chirality with near unity CD is observed while maintaining a high *Q*-factor[101]. A high-index substrate can also break the out-of-plane mirror symmetry implicitly. Indeed, by carefully optimizing the planar structure and engineering the interaction with the substrate, a chiroptical response can be observed[162]. Remarkably, a near-perfect CD (~0.93) was demonstrated by tuning the in-plane geometries[60]. Apart from breaking the structural symmetry, it was postulated circular eigenstates can also be realized by breaking the time-reversal symmetry. The magneto-optical coupling cause Zeeman splitting, giving rise to circular eigenstates[163]. The advantage of such scheme is that the chirality of the states can be switched by the magnetic field while preserving the structural symmetry, thus higher *Q*-factors.

A unified framework for describing chirality in any BIC cavity can be established using coupled-mode theory where the cavity fields can be decomposed into two components $\boldsymbol{P} = [p_{\mathrm{LCP}}, p_{\mathrm{RCP}}]$. The dynamical evolution of these components, including their interaction with external radiation, is governed by the coupled-mode equations:

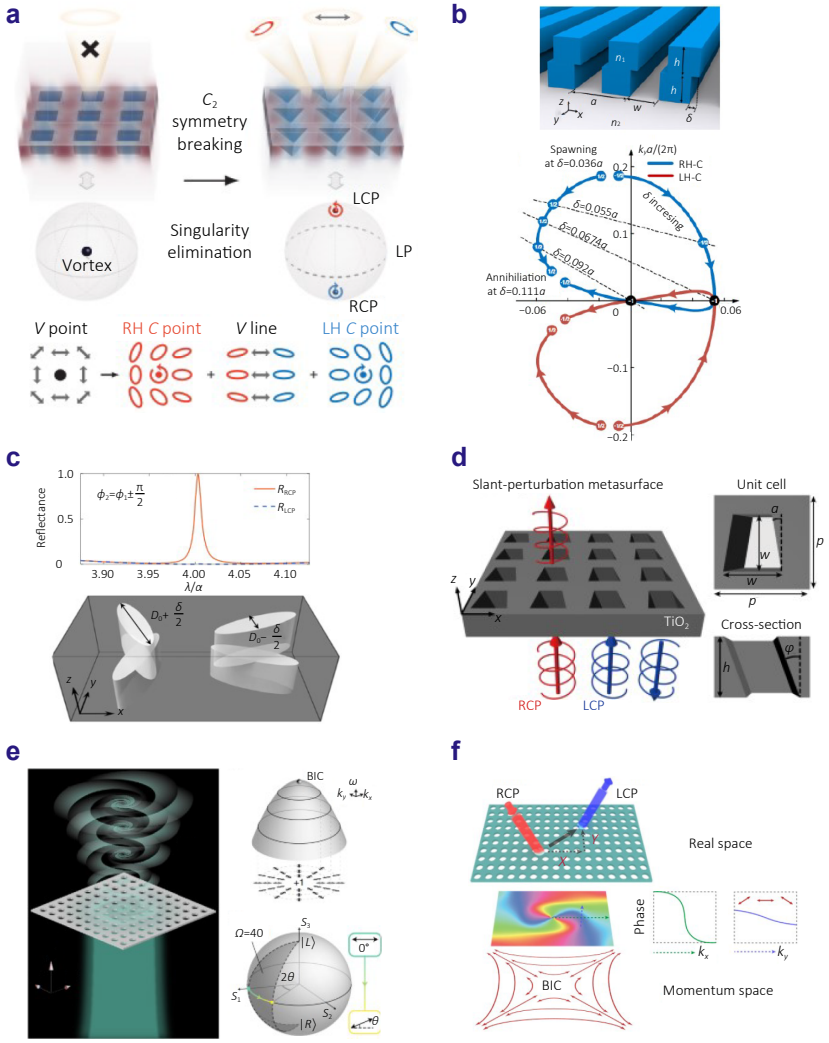


Fig. 4 | (a) Perturbing the in-plane C_2 symmetry breaks the *V*-point into a pair of *C*-points and an *L*-line. (b) The trajectory of generation, annihilation, and combination of *C*-points for a grating when the geometry varies. (c) Chiral quasi-BIC states by stacking two layers with different rotation angles. (d) Observation of high CD intrinsic BIC by slanted structures breaking all symmetries. (e) Optical SAM-OAM conversion by taking advantage of the topological vortex in k-space. (f) Spin-Hall effect by the topological vortex around the BIC point. Figure reproduced with permission from: (a) ref.[152], under a Creative Commons Attribution License; (b) ref.[132], American Physical Society; (c) ref.[155], American Physical Society; (d) ref.[101], Springer Nature; (e) ref.[126], Springer Nature; (f) ref.[127], American Physical Society.

$$\frac{\mathrm{d}\boldsymbol{P}}{\mathrm{d}t} = \left[\mathrm{i}\left(\omega - \omega_0\right) - \gamma_0\right]\boldsymbol{P} + \boldsymbol{M}\boldsymbol{a}\,, \tag{7}$$

$$\boldsymbol{b} = \boldsymbol{N}\boldsymbol{P} + \boldsymbol{C}\boldsymbol{a}\,, \tag{8}$$

where $\boldsymbol{a} = [a_{\mathrm{LCP}}, a_{\mathrm{RCP}}]$ and $\boldsymbol{b}$= $[\mathrm{b}_{\mathrm{LCP}}, \mathrm{b}_{\mathrm{RCP}}]$ denote the amplitudes of the incoming and outgoing radiation channels, respectively. The matrices $\boldsymbol{M}$ and $\boldsymbol{N}$ describe the coupling of the incident waves into the cavity mode and the radiation emitted from the mode. Their elements are constrained by time-reversal symmetry and reciprocity.

The matrix $\boldsymbol{C}$ represents the direct (non-resonant) scattering pathway between the incident and outgoing waves. Its values can be obtained by modeling a uniform slab with the same average material properties; importantly, the $\boldsymbol{Ca}$ term does not introduce any chirality.

Chiral responses arise from engineering the elements of $\boldsymbol{M}$ and $\boldsymbol{N}$ such that one helicity becomes selectively decoupled from the radiation channel. BICs are particularly advantageous for achieving strong chiral behavior because their modes are naturally decoupled from radiation for both helicities. Therefore, one only needs to symmetry-breaking to enable coupling of a single helicity to the radiation continuum. Table 3 summarizes recent experimentally demonstrated chiral metasurfaces across different wavelength regimes.

A time-even pseudoscalar called optical chirality can be used to quantize the asymmetry of the interaction electromagnetic field with chiral molecules[169]:

$$\boldsymbol{C}=\frac{\varepsilon_0}{2}\boldsymbol{E}\cdot\nabla\times\boldsymbol{E}+\frac{1}{2\mu_0}\boldsymbol{B}\cdot\nabla\times\boldsymbol{B}\,, \tag{9}$$

where ε_0 and μ_0 are the vacuum permittivity and permeability, and $\boldsymbol{E}$ and $\boldsymbol{B}$ are the time-varying electric and magnetic fields. The optical chirality quantitatively describes the excitation rate of chiral molecules when placed in a chiral EM field. For plane waves in free space, the maximum chirality of a circularly polarized light is $C_{\rm CPL}=\pm 2U_e\omega/c$, where c is the speed of light, ω is the frequency of light, and ± represents the chirality of left-handed and right-handed circularly polarized light, $U_e=\varepsilon_0|\boldsymbol{E}|^2/4$ is the time-averaged electric energy density[170]. It is shown that Maxwell's equation allows the existence of superchiral fields, whose chiral asymmetry is higher than that of circularly polarized light, i.e. $|C/U_e|>2\omega/c$[170]. Superchiral fields can be easily achieved in the near field because the evanescent field allows much higher spatial frequencies than in the free space. Quasi-BIC modes are found to be efficient superchiral near-field generators due to the high Q-factor which enhances near-field interaction. By exciting x- and y-polarized quasi-BIC modes simultaneously, a strong superchiral near field contributing to a ~59 times enhancement of CD signal is observed by numerical simulation[145]. Another study shows each isolated BIC has a $C/C_{\rm CPL}$~10, and this value can be enhanced by almost two orders of magnitude when the TE and TM BIC merge[171].

The topological vortex in the k-space also gives rise to strong photonic spin-Hall effects. It is shown theoretically that the spin angular momentum (SAM) can transfer to orbital angular momentum (OAM) via the interaction with a BIC of a periodic array of dielectric spheres[172]. Subsequently, this is demonstrated experimentally by impinging circularly polarized light onto a photonic slab (Fig. 4(e)). The rotation of the polarization field around a BIC point can exert a Pancharatnam-Berry phase upon interaction with the cross-polarized part of the incoming circularly polarized light[126]. In this case, the metasurface is not required to have chiral geometry. Instead, the chirality is mediated by the vortex in the k-space. This k-space Pancharatnam-Berry phase can also manifest in the nonlinear regime. The third- and fifth-harmonic excited by circular polarization is shown to have $\sigma(n\pm1)q$ topological charge, where q is the polarization charge of the BIC, n is the order of harmonics, and σ is the polarization state of the excitation light[173]. The spin-polarized directional coupling of the evanescent waves in a BIC mode is also observed when excited by a circularly polarized beam at normal incidence[174]. At oblique incidence, it is found that the spin-dependent beam shift can happen in both lateral directions (Fig. 4(f)) due to the combination of the Pancharatnam-Berry phase and resonant phase gradient inflicted on the cross-polarized light[127].

3.4 Flatband BICs

The concept of the Moiré superlattice was first developed in the context of twisted bilayer graphene or other van der Waals heterostructures. These structures arise when two layers of material with similar periodic arrangements are stacked with a slight twist or misalignment, resulting in new periodic patterns and unique properties. In a similar manner, Moiré superlattices can be generated within photonic systems by superimposing two periodic photonic structures that have slight variations either in their lattice constants or in their orientation[175–179]. Under the specific interlayer coupling and twist angles, a flatband can be formed in this system. In the flatband regime, light becomes highly localized, often concentrated in specific regions of the superlattice[180]. In addition, the effective mass of photons, calculated by $m^*=\hbar^2/\frac{{\rm d}^2E}{{\rm d}k^2}$, increases significantly in the flatband, causing the light to propagate more slowly through the structure. This slow light effect further increases the light-matter interactions, thus benefiting the lasing[176–178], nonlinear optics[181] and chirality[182–185]. In electronic Moiré superlattices, a nondispersive flatband typically forms at the Brillouin zone corner, originating from the Dirac cone under small twist angles. As such, most Moiré flatbands in

Table 3 | Summary of chiral dichroism in BIC cavities.

CD	Q-factor	Spectral range	References
0.67	938	3–9 μm	ref.[161]
0.85		3.3 μm (~9 GHz)	ref.[156]
0.985	3258	2 μm (~ 0.13 THz)	ref.[164]
0.8		1400–1700 nm	ref.[165]
0.93	1835	1400–1550 nm	ref.[60]
0.812		1560–1620 nm	ref.[166]
0.93	2663	615–620 nm	ref.[101]
0.925	1250	580–640 nm	ref.[102]
0.98	2100	580–588 nm	ref.[167]
0.99	10037	520–560 nm	ref.[168]
0.7	~50–110	500–1000 nm	ref.[159]

photonic systems lie below the light line, whereas BIC must exist above the light line in photonic crystal systems[186].

Recently, Huang et al. introduced the concept of a Moiré quasi-BIC above the light line[186]. They demonstrated that as the twist angle decreases, the Moiré quasi-BIC flatband approaches and can eventually converge with a true BIC (Fig. 5(a)):

$$\begin{aligned}
&\boldsymbol{H}_{\text{Moiré}} = \begin{pmatrix} H_1 & V_0 & V_0 \\ V_0 & H_2 & V_0 \\ V_0 & V_0 & H_3 \end{pmatrix}, \\
&\boldsymbol{H}_{\xi} = \begin{pmatrix} \omega_0 + b\,(\boldsymbol{k} - \boldsymbol{G}_{\xi}) & U \\ U & \omega_0 + b\,(\boldsymbol{k} - \boldsymbol{G}_{\xi}) \end{pmatrix}, \\
&\boldsymbol{V}_0 = \begin{pmatrix} 0 & V \\ V & 0 \end{pmatrix}. \qquad (10)
\end{aligned}$$

By constructing the analytical model of Moiré photonic crystals at the center of the first order Moiré Brillouin zone, the authors found that the flatband above the light line can be achieved by controlling the interlayer coupling strength and the twist angle (Fig. 5(b)). The far-field radiation polarization states of twisted bilayer photonic crystals exhibit singularities at the Γ-point. Additionally, the Q-factor of the Moiré band decreases as the twist angle increases, as shown in Fig. 5(c). These characteristics clearly indicate that the Moiré flatband is a quasi-BIC.

Figure 5(d–f) present theoretical analyses and simulation results, demonstrating that twisted photonic crystals not only produce flatbands but also give rise to other intriguing phenomena, such as optical vortices[187]. These findings highlight the broader potential of twisted photonic structures in manipulating light in novel ways. Under the zero-twist angle, BIC modes in each photonic crystal layer are isolated from the free space radiation. When a small twist angle is induced to generate Moiré superlattice, the BIC mode in one photonic crystal can interact with the guided mode in the other photonic crystal and couple to far-field radiation. In k-space, the polarization states of the BIC band near the Γ point exhibit a vortex structure. Based on temporal coupled-mode theory (TCMT) calculations, the output radiation electric field can be decomposed into left-handed and right-handed components. Both left-handed and right-handed light acquire a Pancharatnam-Berry phase, which is opposite for each component and depends on the polarization angle of the guided mode. Thus, the output field will obtain the spiral phase front at real space whose topological charge is equal to the BIC mode (the positive and negative topological charges for the left-handed and right-handed light basis). The production of vortex light is robust against the incident light beam such as incident angle or incident position.

Because of the inherent complexity involved in the fabrication process, experimental investigations of Moiré BIC cavities have been limited. The intricate nature of the multi-step lithography process with high precision required has posed significant challenges, thereby limiting experimental research on Moiré BIC cavities. A good strategy to experimentally achieve moiré structure is by merging two layers of nanostructure into a single layer, which can overcome this nanofabrication limitation[188]. Very recently, Qin et al. experimentally demonstrated the optical Moiré BIC in the 1D grating system (Fig. 5(g–i))[189]. Interestingly, several diffraction channels with different orders and topological charges at momentum space are detected. This study claims the high Q-factors of ~6051 and ~1094 at the angle of 6.4° and 8.3°, respectively and attributes to the combined influence of band folding induced by the Moiré potential and multiple topological charges. The ultrahigh Q-factors of flatband Moiré BIC span over a much wider range of angles compared to conventional BICs. In addition, these Moiré superlattice cavities offer an ultrasmall mode volume while maintaining a high Q-factor[185], making them highly efficient for laser applications.

Another promising approach for generating flatband BICs is engineering strong interaction between photonic bands, as demonstrated in Fig. 5(j–k)[191]. In this one-dimensional photonic crystal system, vertical symmetry is broken by retaining an unpatterned slab, allowing odd-like and even-like modes to couple. Two FW-BICs emerge near the anti-crossing point, and a symmetry-protected BIC exists at the Γ-point and at the same energy. By adjusting the filling factor, FW-BICs shift toward the Γ-point, while symmetry-protected BIC remains. When the filling factor reaches a critical value, the 3 BICs merge, boosting the Q-factor of the off-Γ states and resulting in the formation of a flatband BIC. The dispersion surfaces evolve from a saddle shape before merging, to an ultraflat band during the transition, and finally to a paraboloid surface after merging. Different from the BIC-merging to form super-BIC, this work can manipulate both the real and imaginary parts of the band structure to achieve a high-Q flatband.

Using a similar concept of merging photonic modes with opposite curvatures, very recently, Do et al. demonstrated room-temperature lasing from flatband BIC by precisely controlling the interaction between counter-propagating guided modes along the x- and y-directions with different group velocities[190]. This is achieved by varying the anisotropy of a two-dimensional lattice of nanopillars. This flatband BIC, characterized by an extremely low group velocity, a high density of states, and the 100-fold enhancement of the Q-factor over a wide range of angles along the merging direction (y-axis) (Fig. 5(l)) significantly enhances the interaction between photons and gain media, thereby amplifying the stimulated emission rate. As the final result, the lasing threshold for flatband BIC decreases by a factor of four compared to symmetry-protected BIC lasing in the square lattice (Fig. 5(m)).

3.5 Strong light-matter interaction and BIC polaritons

Light-matter interaction that modifies the properties of the

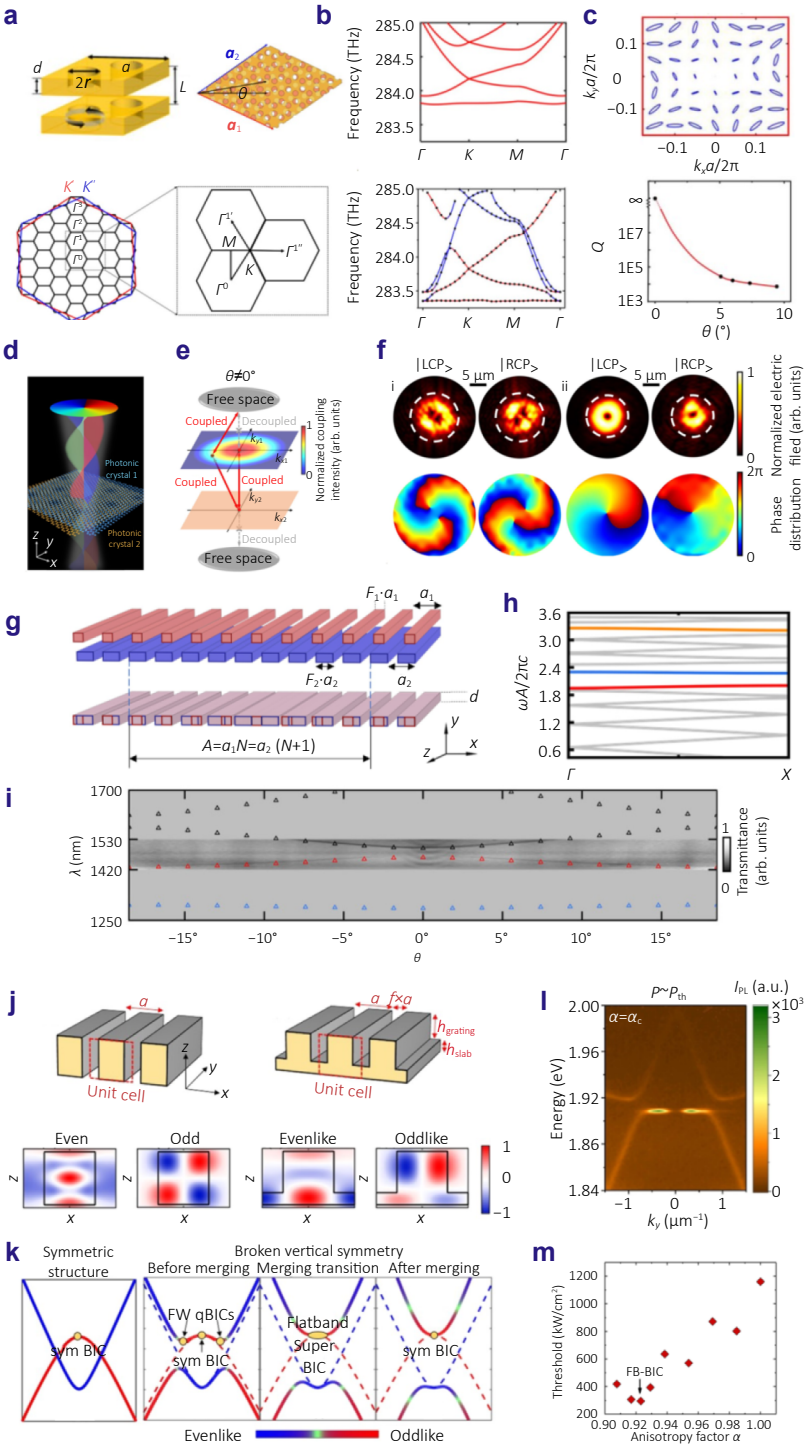


Fig. 5 | (a) Top panel: schematic diagram of twist bilayer photonic crystal. Bottom panel: the Moiré Brillouin zone. (b) Band dispersions are calculated by analytic model and numerical simulation. (c) Top: far-field polarization states map at momentum space. Bottom: *Q*-factor of Moiré quasi-BIC band against the twist angle. (d) Schematic diagram of twist bilayer photonic crystal that produces optical vortex. (e) Interlayer coupling mechanisms of twist bilayer photonic crystal. (f) Top: amplitude of left-handed and right-handed emissions at far-field. Bottom: phase distribution of the corresponding mode. (g) Design of 1D Moiré PhC slab, two-layer grating merge into a single layer. (h) Simulated band structure of 1D Moiré PhC slab. (i) Experimental angle-resolved transmission spectra. (j) Comparison of up-down symmetry structure and up-down symmetry broken structure. The up-down symmetry broken allows the interaction between odd-like and even-like modes. (k) Bands dispersion under the different configurations with the flatband achieved at the merging condition. (l) Lasing at flatband BIC whose threshold is 4 times lower than that at the symmetry-protected BIC in a standard square lattice (m). Figure reproduced with permission from: (a–c) ref.[186], American Physical Society; (d–f) ref.[187], Springer Nature; (g–i) ref.[189], Springer Nature; (j, k) ref.[191], American Physical Society; (l, m) ref.[190], American Chemical Society.

individual states, plays crucial roles in the development of fundamental science and novel optoelectronic devices and quantum applications. In the weak coupling regime, the fluorescence is enhanced by Purcell effects. On the other hand, strong coupling leads to the creation of hybrid states of light and matter since the excitons and photons coherently exchange energy. The new hybrid states are called polaritons—a bosonic quasi-particle, energetically separated by a characteristic Rabi splitting. Thanks to the half-light half-matter nature, polaritons inherit all the properties of the excitons (strong nonlinearity, strong interparticle interaction) and of the photons (low mass, fast propagation). The contribution from each component to the polariton states, known as Hopfield coefficients, can be controlled that allows for the engineering of the polariton-polariton interactions. The exciton polaritons physics was first introduced in 1958 by Hopfield for bulk systems[192] and for quantum systems by Andreani et al.[193,194], and has been an active research topic until now because of the exciting physics such as polariton bistability, Bose-Einstein condensation (BEC), topological edge state, quantum vortex, ultrafast transport and superfluidity.

Importantly, polariton lasing, which works based on the accumulation of polariton population in ground states via relaxation, does not require population inversion[195] that, in principle, leads to thresholdless lasing or even condensation. However, in practice, the photon loss due to the limited *Q*-factor of the optical cavities, the material loss due to environmental perturbations (temperature, humidity, pumping conditions) increase the required initial polariton density. Therefore, engineering cavity loss is crucial. Compared with, for example, Fabry-Perot, hemispherical and plasmonic cavities, BIC cavities supported by low-loss dielectric metasurfaces have great advantage because of their intrinsically high *Q*. More interestingly, via strong coupling, exceptional properties of BIC photons such as long lifetime (hence, long propagation) and topological nature can be transferred to the BIC polaritons, highlighting the advantages of BIC polaritons over standard exciton polaritons.

Exciton polaritons in BIC cavities have been studied both theoretically and experimentally on a wide range of excitonic materials. Angle-resolved spectroscopy is the most direct technique to probe the polariton branches[196]. A strongly coupled system has been theoretically proposed that involve two-dimensional materials WS_2 on silicon nitride metasurface with the Rabi splitting of 28.4 meV[197]. Stronger splitting of ~160 meV has been calculated in a WS_2 guided mode resonance with the WS_2 grating on top of a WS_2 slab[39] and a monolithic WSe_2 metasurface[198]. Koshelev et al. theoretically studied a system comprising a monolayer WSe_2 on top of an 1D photonic crystal made of Ta_2O_5 grating structure[199]. The Rabi splitting is in the range of 15–100 meV. More importantly, due to the long lifetime of BIC photons, the exciton-polariton lifetime can be enhanced by 100-fold. The proposed scheme has then been experimentally realized using the same BIC cavity and $MoSe_2$ where a splitting of 25 meV has been resolved[200]. Interestingly, by modifying the one-dimensional grating structure fabricated on top of a WS_2 monolayer, replicas of the BIC polariton in momentum space and their nonlinear properties have been observed[201].

Monolithic metasurfaces, where excitons in a material couple with the BIC mode supported by the metasurface made of the same material, show great potential for achieving strong exciton-photon interaction. Dang et al. reported the observation of BIC exciton polaritons at room temperature on a two-dimensional (2D) perovskite subwavelength metasurface with a giant Rabi splitting of ~200 meV[49]. In another monolithic 2D systems using transition dichalcogenides, Weber et al. fabricated WS_2 nanorods metasurface and resolved a Rabi splitting of 116 meV[40]. The authors also demonstrated the tunability of the BIC wavelength across a wide range of 700–850 nm by varying the WS_2 rod size (Fig. 6(a, b)).

Inheriting the infinitely long lifetime of BIC photons, BIC polaritons has prolonged lifetimes compared to the uncoupled exciton states that can serve as ground state for BEC. The first experimental demonstration of the BEC polariton condensation in BIC cavities has been reported in an 1D grating structure made of multi-quantum-well GaAs heterostructure (Fig. 6(c))[68]. The authors first observed the polariton branches evidenced by the Rabi splitting of ~13 meV at cryogenic temperatures (~4 K). When increasing the optical pumping, two-lobe emission is revealed that becomes dominant at high powers (Fig. 6(d)). The nonlinear power-dependent intensity, blueshift are typical signature of a BEC. The condensation threshold is only in the range of a few μJ/cm^2 which is an order of magnitude lower than the weak coupling limit. A similarly low threshold for polariton condensation has been observed in silicon metasurface where the silicon Mie resonators strongly coupled with organic perylene dye molecules[202]. By using perovskite photonic crystal lattice, Wu et al. achieved room-temperature BEC of BIC polaritons at the threshold of ~10 μJ/cm^2 [203]. A large Rabi splitting of above 150 meV, long-range coherent time of ~2.14 ps have been observed experimentally. These BIC polaritons generally have positive masses, strongly repel each other leading to fast expansion of their polariton condensates.

By creating an attractive potential in the gain area through structured pumping profile, polariton condensates can be spatially trapped and evanescently coupled with each other. The coupling between two polariton condensates results in hybridized modes, resembling bonding and antibonding states in molecules (Fig. 6(e)). The mechanism can be scaled up to 10 interacting BIC polariton condensates along an one-dimensional (1D) array (Fig. 6(f)) and in a staggered lattice that enables large-scale reconfigurable many-body systems and especially the generation of multiple optical vortices and vectorial coherent light sources[204].

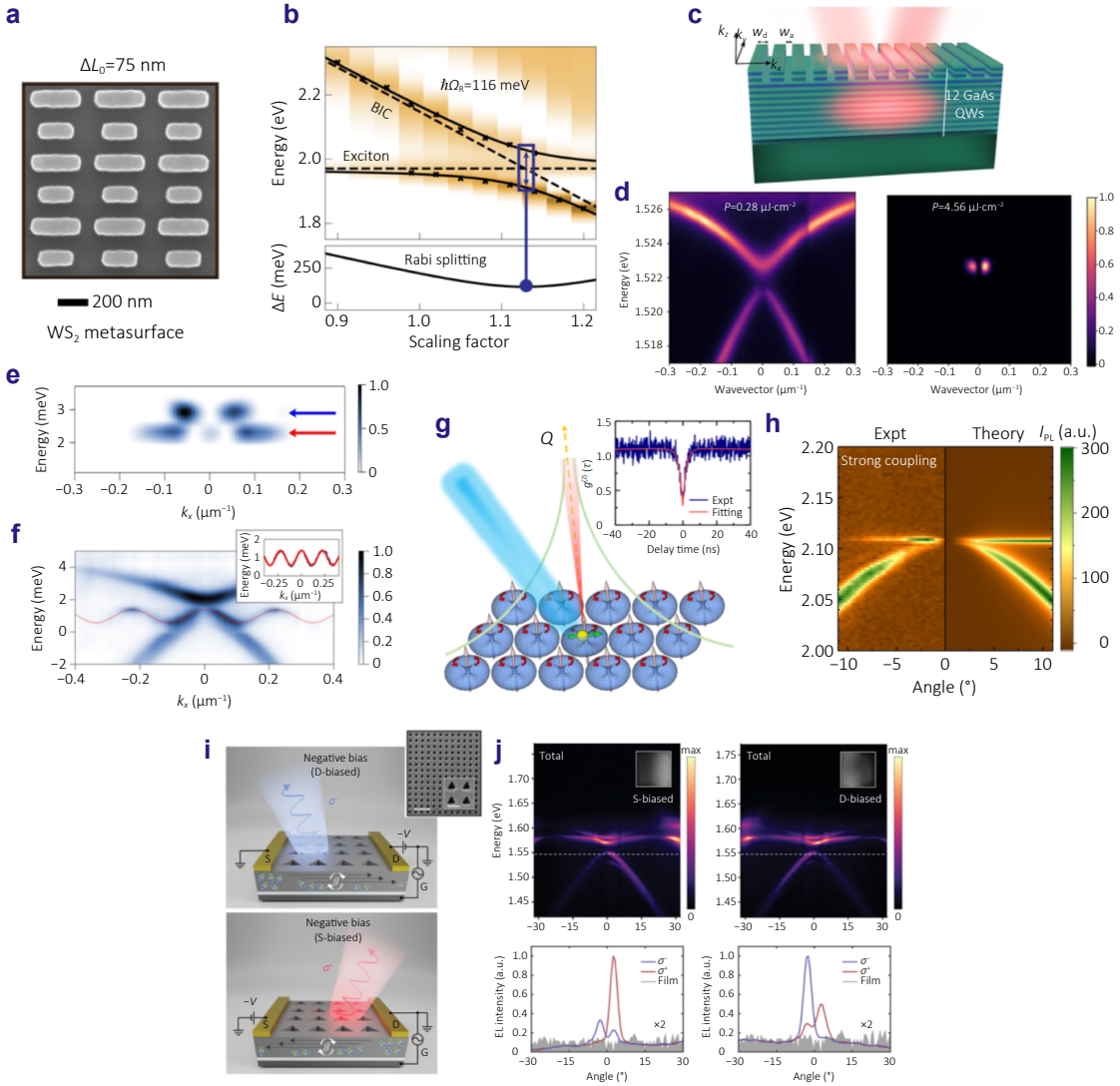


Fig. 6 | (a) Scanning electron microscope (SEM) image of the WS_2 metasurface comprising of rod-like WS_2 nanopatterns. (b) Strong coupling between excitonic and BIC photonic mode in a monolithic WS_2 metasurface with Rabi splitting of ~116 meV. (c) Schematics of a planar GaAs waveguide structure on top of the GaAs quantum-well. (d) Strong coupling with Rabi splitting of ~13 meV and polariton Bose-Einstein condensation of the BIC polaritons. (e) Realization of polariton molecules with bonding (red arrow) and antibonding states (blue arrow) at above threshold. (f) Experimental dispersion spectra of the coupled system of 10 polariton condensates. (g) Schematics of single-photon emitter in a dielectric metasurface. Inset: Antibunching dip showing single-photon emission. (h) Room-temperature strong coupling achieved between a single photon emitter and BIC cavity. (i) Design and SEM image of perovskite metatransistor. (j) Electrically tuned polariton chirality and directionality. Figure reproduced with permission from: (a, b) ref.[40], Springer Nature; (c, d) ref.[68], Springer Nature; (e, f) ref.[204], Springer Nature; (g, h) ref.[205], under a Creative Commons Attribution License; (i, j) ref.[207], John Wiley and Sons.

Achieving strong coupling in strong excitonic materials is relatively straightforward. Moving down to the small molecules or single-photon emitter regime is challenging. Here, the requirements for strong coupling become more stringent, where not only the cavity needs very high *Q*-factor but also the emitter needs to have small decay rate, or equivalently narrow linewidth. Do et al. have demonstrated that by exploiting the fundamentally high *Q*-factor of BIC cavities, strong coupling regime can be reached down to a single photon emitter level[205]. Single-photon emitters generated on a hexagonal boron nitride strongly couple to the BIC mode originating from the vertical magnetic dipole mode supported by TiO_2 nanostructures (Fig. 6(g)). A Rabi splitting of up to ~4 meV has been observed at room temperature (Fig. 6(h)) which is an order of magnitude larger than that reported for the strong coupling regime using single InAs/GaAs quantum dots.

Besides exciton-polaritons, the strong coupling between the vibrational mode of PMMA molecules and BIC mode supported by germanium elliptical nanopillars in infrared wavelengths (5–6 mm) has been theoretically predicted, with a Rabi splitting of ~5 meV[73,206]. By tuning the PMMA layer

thickness, the BIC resonance can be varied across the vibrational mode of PMMA molecules, hence the coupling strength can be controlled.

Notably, in a BIC metatransitor architecture with broken in-plane and out-of-plane inversion symmetry (Fig. 6(i)), Wang et al. demonstrates the generation and controllability of the BIC polariton spin based on the Rashba effects in perovskite materials (Fig. 6(j))[207]. Under negative bias, excitons with opposite spins propagate along opposite directions, preferentially toward the source electrode (drain electrode) under the S-biased (D-biased) condition. This work demonstrates the significant advantages of monolithic metasurfaces design, where the unconventional properties of the active materials (e.g. spin-orbit coupling, Rashba effects) enable active tuning of the light-matter interaction.

Recent rapid progress on BIC polaritons across a variety of material systems has proved the robustness of BIC cavities in achieving strong coupling, polariton lasing and polariton condensation, especially in quantum-confined systems and even down to single-photon emitter level. This capability enables exploration of novel physics in quantum-regime. Together with the development of new quantum sources, coherent energy exchange between stable qubits at room temperature is highly desirable for future quantum technology applications that could be achievable with BIC polaritons.

3.6 Ultrafast phenomena in BIC cavities

The ability to engineer high-*Q* resonances, enabled by the concept of BIC, has advanced their application in studies of ultrafast phenomena, including all-optical switching. All-optical switching uses an optical control pulse to modulate a separate optical signal. The control pulse induces a transient change in the material properties of the system, and the signal passing through it experiences modulation as a result[208]. In contrast to electrically driven optical switching, which is actuated by an applied voltage or current and operating at GHz speeds, optical triggering can support fully optical signal processing and achieve ultrashort switching times defined by the duration of the triggering pulse, which can be as short as tens of femtoseconds[209]. However, all-optical switching remains largely at the research stage, since achieving large modulation depth, low energy consumption, and ultrafast switching time in the same system is challenging. While electro-optic modulators can reach modulation depths of 45 dB[210], ultrafast all-optical switching is typically limited to below 20 dB, hindering their practical applications[211]. The modulation-depth limitation can be mitigated by using high-*Q* resonances such as quasi-BICs. When the *Q*-factor of a resonant structure is sufficiently high, even small changes in material properties can lead to substantial modulation depth at a chosen wavelength[211–214].

Mechanisms for altering material properties on picosecond and subpicosecond timescales, commonly referred to as ultrafast, include optically induced free carrier injection and third-order nonlinearities. Ultrafast switching via free-carrier injection in BIC metasurfaces has been experimentally demonstrated in various spectral ranges, including the near-infrared with a GaAs metasurface[215], the mid-infrared with an amorphous Ge metasurface[216], and terahertz with Si and hybrid metasurfaces[76,217,218]. An alternative approach through third-order nonlinearities offers faster, pulse-limited switching but generally results in lower modulation efficiency compared to free carrier injection[219]. However, a recent study employing a pump at an optimized wavelength to maximize the nonlinear response has demonstrated competitive modulation performance[220]. In this study, as illustrated in Fig. 7(a), a BIC metasurface composed of amorphous Si disks on a mirror achieved 22% reflectance modulation on a pulse-limited timescale with a pump fluence as low as 255 μJ/cm^2, highlighting its potential for fast and efficient all-optical switching. While this modulation depth is still significantly lower than that of electro-optic modulators, its ultrafast switching time of 100 fs shows the unique advantage of the all-optical approach. By optimizing the material choice, the energy consumption and modulation depth can be further improved[221]. Finally, in addition to intensity modulation, recent studies have demonstrated the potential of BIC metasurfaces for ultrafast switching of the polarization state[222] and orbital angular momentum[223].

When the tuning of an optical cavity occurs on a timescale similar to or faster than the photon lifetime in the cavity, the spectral characteristics of the light captured in the cavity can change. In quasi-BIC resonances characterized by high *Q*-factors, optical metasurfaces provide photon lifetimes long enough to observe spectral modification effects when the structure is externally modulated on a sub-picosecond timescale. In a recent experimental study, linear frequency conversion was observed in a GaAs metasurface with a symmetry-protected quasi-BIC when it was rapidly shifted due to optically induced free carrier injection[224]. In the transient transmission spectrum, as shown in Fig. 7(b), frequency conversion is revealed at negative pump-probe delays, where the probe arrives first and couples into the metasurface at the unperturbed resonance frequency. When the pump subsequently arrives, it shifts the resonance, causing the frequency of the light captured in the resonance to change. Interferometric fringes then arise due to the interference between the frequency-shifted light and the light that has not coupled to the metasurface mode. When the light undergoing frequency conversion is used to generate harmonics, this effect causes the harmonic frequencies to no longer be integer multiples of the original pump frequency. This was experimentally demonstrated in two scenarios: first, when the pump intensity was high enough to cause a self-induced shift in the resonance position[227], and second, with an externally modulated metasurface, where the resonance was rapidly shifted by an additional control pulse[228].

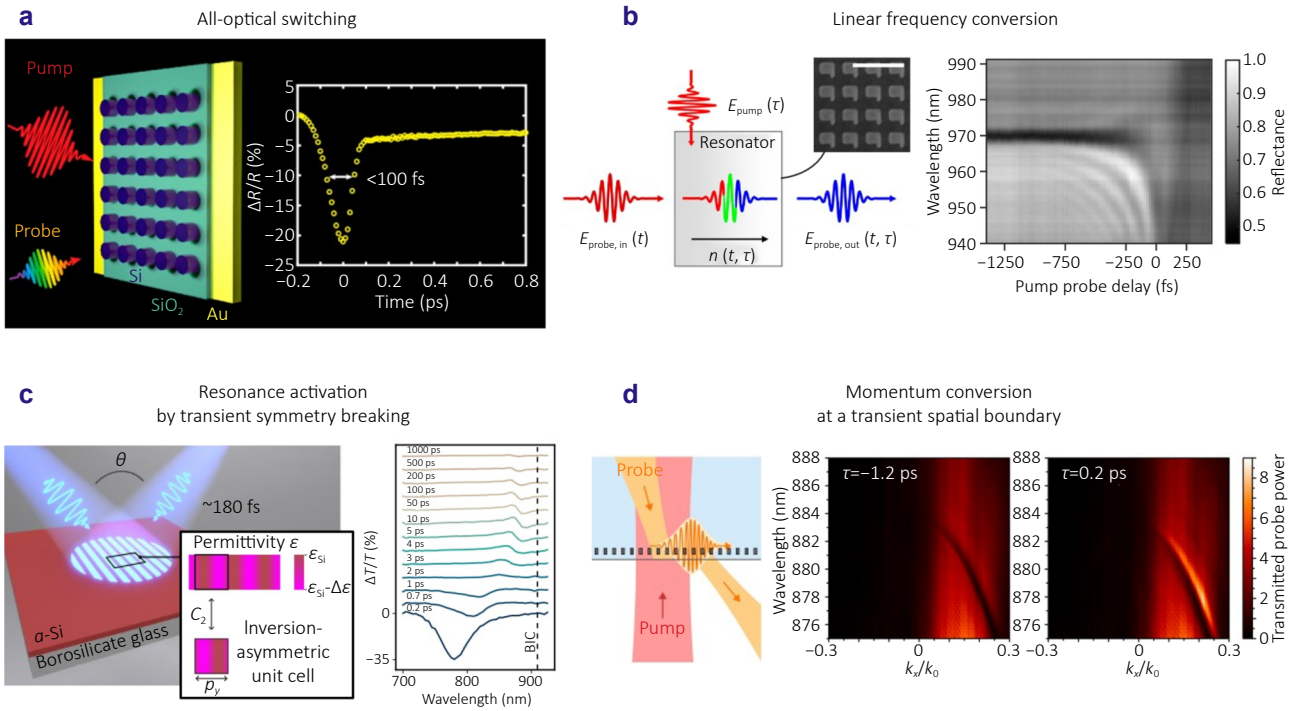


Fig. 7 | (a) All-optical modulation enabled by a mirror-induced BIC; transient reflectance at a pump fluence of 255 μJ/cm² is shown in the inset. (b) Linear frequency conversion in a time-variant GaAs metasurface, manifested as interferometric fringes at negative pump-probe delays. (c) Transient symmetry breaking induced by structured pumping of a featureless silicon film, resulting in the emergence of a quasi-BIC resonance. (d) Spatially selective ultrafast modulation of a GaAs BIC metasurface leading to momentum conversion at the transient spatial boundary between pumped and unpumped regions. Figure reproduced with permission from: (a) ref.[220], under a Creative Commons Attribution License; (b) ref.[224], American Chemical Society; (c) ref.[225], Springer Nature; (d) ref.[226], American Chemical Society.

If radiative coupling with the far field can be dynamically altered to switch between a quasi-BIC and a perfect BIC, an intriguing opportunity arises to break the time-bandwidth limit. This limit refers to the constraint in any time-invariant cavity, where one cannot increase the cavity bandwidth without proportionally reducing the storage time of light in the cavity. In time-variant systems, however, this limit does not necessarily hold true. One can capture broadband light into a long-lived resonance if the resonance bandwidth shrinks during the coupling process[229–231]. This capability can be beneficial for multiple applications, including energy harvesting, harmonic generation[232,233], and optical signal buffering[234]. Theoretically, it has been shown that modulating the properties of a cavity according to a suitable temporal law allows the capture of up to 100% of the energy from a broadband pulse into the mode, which ultimately becomes a perfect BIC, achieving infinite photon storage time[235]. Experimentally, this concept has been demonstrated in a system consisting of two coupled Si ring resonators, where the storage time was limited only by nonradiative losses[236].

When ultrafast optical modulation of metasurfaces is studied, they are typically pumped uniformly. However, spatially extended BIC modes in optical metasurfaces may exhibit different phenomena when subjected to spatially non-uniform modulation. This additional degree of freedom —control over the spatial distribution of the pump —could allow for independent tuning of both the resonance wavelength and the *Q*-factor. It has been theoretically shown that a structurally asymmetric GaAs grating, which supports a quasi-BIC resonance, can achieve ultrafast *Q*-factor boosting when subjected to spatially non-uniform optical pumping[237]. In the suggested configuration, the pump was aligned with the individual bars, and the geometrical asymmetry of the structure was compensated through pump-induced selective permittivity changes, resulting in a reduction of radiative losses. Recently, Berté R et al. experimentally demonstrated the ability to control both the resonance position and *Q*-factor of a BIC mode by pumping a featureless amorphous Si film with a periodic intensity distribution[225]. When the film was pumped, the radiative channel opened on a picosecond timescale, temporarily transforming the true BIC state into a quasi-BIC, as shown in Fig. 7(c). The resonance position and *Q*-factor of the emerging resonance were dictated by the spatial period and intensity of the pump. As an example of an application of this system, Berté R et al. demonstrated the enhancement of third-harmonic generation at a specific wavelength within a narrow timeframe.

As an alternative to pumping with a spatially non-uniform

profile, one can design a BIC structure that, when optically pumped, exhibits enhanced absorption in specific regions. This leads to spatially non-uniform free-carrier generation and may also alter radiative losses. Such an approach was used in a recent theoretical work, which showed that when an array of symmetrical AlGaAs nanowires is optically pumped at an inclined incidence, the resulting spatially non-uniform injection of free carriers can break the symmetry and transform a true BIC into a quasi-BIC[238]. In a recent experimental study, an array of asymmetrical silicon dimers was pumped at a wavelength that created a hotspot and enhanced free-carrier generation only in one particle of each dimer, thereby either enhancing or compensating the asymmetry initially introduced by geometry and enabling tuning of the radiative Q-factor[239].

When a structure supporting a symmetry-protected BIC at normal incidence is illuminated at an angle, the BIC turns into a quasi-BIC leaky guided mode that is sensitive to spatially selective modulation. In this case, as recently demonstrated for a GaAs metasurface supporting such a mode, one can achieve both frequency conversion in the pumped areas and momentum conversion at the temporally introduced spatial boundaries between the pumped and unpumped regions[226]. The momentum conversion results in dynamic beam bending: when light arrives with a certain time delay relative to the pump, it couples to the metasurface mode at one angle of incidence and exits at a different angle, as shown in Fig. 7(d). This experiment clearly demonstrated the nonlocal nature of the BIC mode, as modulation was observed even when the pump and probe beams were directed at different parts of the metasurface.

3.7 Exceptional points

Non-interacting and lossless systems such as ideal BIC cavities can be described by Hermitian operators that degenerate at the so-called diabolic point and exhibits pronounced topological effects. When an external perturbation ε is introduced, the eigenvalue splitting is proportional to the perturbation. In contrast, the non-Hermiticity in open systems with radiative losses enables more exotic topological properties that are not present in the Hermitian counterpart. A typical example is the emergent physics of exceptional points (EPs), when both the eigenvalues and eigenfunctions collapse into an orthogonal state to itself. Single EPs[240,241], multiplets of EPs[242] and continuous rings of EPs[243] have been realized in a wide variety of optical systems. Both theoretical and experimental aspects of EPs physics were described in literature[244]. On the other hand, paired EPs and the interplay between them lead to even more exotic physics of bulk Fermi arc[245]. The perturbation-induced splitting scale with $\varepsilon^{1/N}$, where N is the order of the EP[246]. Hence, EPs are more sensitive to small perturbations than diabolic points, whereas higher-order EPs even have higher sensitivity. Experiments have showed that sensing devices based on the EPs concept have double sensitivity[247,248] and lower detection limit by two orders of magnitude[249] compared to diabolic-point sensors.

Exceptional points can be tailored via the detuning, coupling strength and gain-loss ratio between the coupled states. Interestingly, while loss is generally considered as bad for optical cavities, it can be engineered in non-Hermitian systems for novel functionalities. The concept, analytical model and engineering of EPs in different systems have been discussed elsewhere[250–252]. However, designing a non-Hermitian system with BICs coalescing into EPs is challenging that if done, will lead to hybrid EP-BIC states inheriting both the extremely high Q-factor of BICs and the nonlinearity of EPs. For example, theoretical simulation predicted the greatly enhanced density of states (DOS) at EPs ($\sim Q^2$ or higher order) compared to the Purcell factor ($\sim Q$)[253–255]. Therefore, the DOS of the EP-BIC cavities can be orders of magnitude larger than the individual EP or BIC systems that facilitates a wide range of applications such as sensing, lasing and light-matter interaction.

Figure 8(a–c) show the theoretical calculation of the EPs and band inversion of the dielectric guided modes in a perovskite metagrating structures on a metallic plane (Fig. 8(a))[256]. In this system, the interaction between two counter-propagating waves via diffraction mechanism and radiative losses through the continuum gives rise to a bright mode taking all the losses and a dark mode with no loss (quasi-BIC). By tuning the filling factor f, the coupling strength varies from positive to negative and the band inversion is observed. When $\varepsilon = 0$ ($f = 0.51$), the two eigenvalues degenerate, forming two EP-BICs separated in momentum (Fig. 8(b)). Excitons in the active perovskite material can strongly couple to these EPs leading to two pairs of dark/bright upper and lower polariton branches that follow the behaviours of the photonic modes (Fig. 8(c)). Recently, polariton lasing have been experimentally demonstrated at the EPs supported by a similar perovskite metagrating structure[257].

In order to improve the Q-factor of the EP-BICs, Qin et al. proposed a scheme to control the interaction between two BIC modes supported by two waveguide stripes on top of a lithium niobate thin film photonic integrated platform (Fig. 8(d))[258]. By varying the separation between the waveguides, the BIC modes are distorted resulting leaky channels and increased loss rates. Under a critical condition where the eigenvectors coalesce and the two BICs merge, the EP-BIC is formed. The orthogonality of the eigenstates has been evaluated to verify the non-Hermiticity of the system. The loss rate at EP-BIC is 5 orders of magnitude smaller than that at the individual BICs (Fig. 8(e)).

Furthermore, the combination of EP and BICs also offer an efficient way to control the propagation and scattering of light. Deng et al. proposed a metagrating structure comprising of metallic slits supporting localized mode on top of a dielectric layer supporting guided modes (Fig. 8(f))[259]. In the

weak coupling regime, a degenerate line is found (Fig. 8(g)) revealing the emergence of two diffractive EPs in the vicinity of the high-Q state (quasi-BIC). By tailoring the coupling strength between these modes, the wavefront can be effectively shaped as shown in Fig. 8(h). At the BIC resonance condition ($k_0 \sim 1$, middle panels), the reflection happens at the first-order diffraction, whereas ordinary reflection occurs at even slightly off resonance ($k_0 \sim 0.95$ and $k_0 \sim 1.1$).

Several designs show the co-existence of BICs and EPs in the same parameter space; even two pairs (EP + BIC) can be achieved in a very thin ring resonator[242]. Recently, second-order and third-order EP-BICs have been predicted theoretically in multilayer dielectric metasurfaces[260]. Nevertheless, the theory and experiments for the hybrid EP-BIC modes are still limited, partially due to the critical conditions for matching these two different singularities EP and BIC. The connection between the EP pair forms an isofrequency contour called bulk Fermi arc that is topologically protected by the charges of the coupled EPs[245]. The study of EP-BICs will bridge several fields of topological photonics and non-Hermitian physics, in which balancing the gain and loss is a new degrees of freedom to design for lasers with better coherence properties, nonlinear resonators and reconfigurable diffraction surfaces and open up the possibility of topological energy transfer between two devices.

4 Applications of BICs and current progress

4.1 Lasing

The first BIC laser is demonstrated in an InGaAsP multiple quantum wells structure with only 8-by-8 nanoresonators[20]. Lasing is subsequently demonstrated with colloidal quantum dots[35,36], dye materials[135], suspended GaAs[261], GaN[32] and halide perovskites[262]. These lasing experiments demonstrated the topological singularity nature of the BIC states by analyzing the far-field pattern of the emission. Compared with semiconductor edge-emitting and surface-emitting lasers which typically emit light in the normal direction to the mirror surface, BIC lasers can be controlled with the flexibility to emit in a wide range of directions by deliberately increasing the periodicity in one direction to introduce

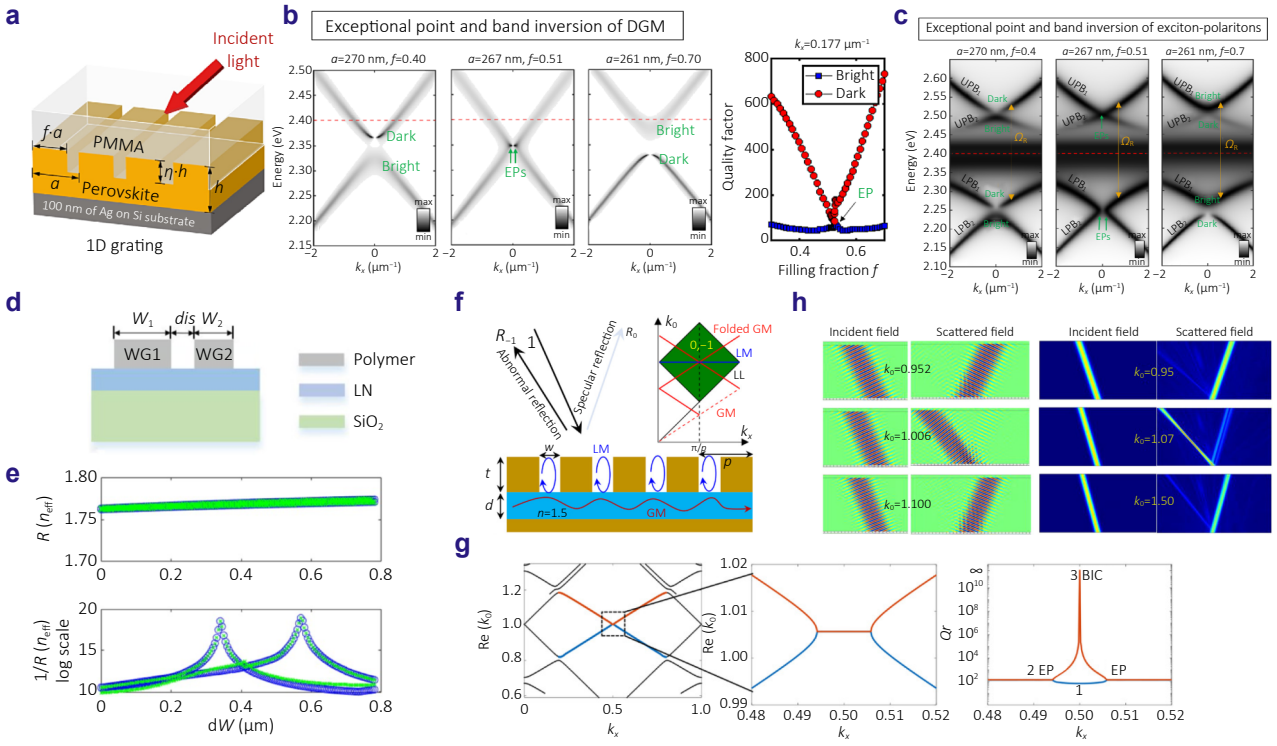


Fig. 8 | (a–c) Strong exciton-photon coupling with the dielectric guided mode (DGM) in perovskite metasurfaces. (a) By varying the diffracting coupling strength, the band inversion and the exceptional points are observed in both (b) passive and (c) active structure. (d) Ultralow-loss EP by coupling two BICs (dual-BIC scheme) in a coupled polymer waveguide system. By engineering the mode profiles and mode coupling strength, EP-BIC is formed with the reduced loss rate revealed in the imaginary part of the refractive index function plotted in (e). (f) Unitary diffraction efficiency on metagrating composing of metallic slits supporting localized modes and a dielectric layer supporting guided modes, obtained by using the concept of BICs and EPs. (g) Band diagram of the real part of the specular reflection wavevector k_0 versus parallel wavevector k_x and quality factor. (h) Wavefront shaping leveraging EPs in the diffractive regime. Figure reproduced with permission from: (a–c) ref.[256], Chinese Laser Press; (d, e) ref.[258], under a Creative Commons Attribution License; (f–h) ref.[259], John Wiley and Sons.

a radiation channel to the BIC mode[65], by FW-BIC[96,262]. It is also possible to obtain multiple-beam output when both symmetry-protected and accidental BIC resonance are involved in lasing[42].

A fundamental limitation of single-BIC cavities is, despite the high-Q at the BICs, the fast decay of Q-factor as moving away from BIC conditions due to the scattering to the neighboring k-point[263,264]. To suppress the out-of-plane radiation and lateral scattering, merging multiple BICs into a single super-BIC mode[70] and combining BICs with lateral confinement in quantum materials[261,265] can boost the Q-factors by orders of magnitude. As a result, ultra-low threshold lasing have been successfully obtained with the record value of ~0.052 kW/cm^2 in a 7×7 unit cell (~3.5×3.5 mm^2) device under continuous-wave (CW) pumping that works up to 70 °C[265], and even electrically pumped lasers with an ultra-compact cavity size (~2λ to 3λ) have been demonstrated in the THz range[80,266]. The lasing threshold largely depends on the stability of gain media against high temperature, humidity and strong pumping conditions. Especially for BIC lasers made of soft materials such as perovskites and colloidal quantum emitters, the material stability needs further optimization.

Besides lowering the lasing threshold, the high-Q BIC cavities are also used to increase the coherence of microlasers. By strategically placing the gain medium in the waveguide, the photons dwell in the low-loss nanocavity for a longer time, which counteracts the phase diffusion in the gain medium, leading to a longer coherence time, up to 20 times smaller linewidth than the previously reported microlaser[267]. Furthermore, BICs provide huge potential for vortex beam manipulation because they inherit the topological polarization state that facilitates the generation of vector beams. Vortex microlasers based on BIC was demonstrated on several systems such as perovskite photonic crystal waveguides[134] and dye-TiO_2 lattice[268]. Ultrafast switching between beam profiles with the switching time of ~1 to 1.5 ps and a record low power consumption are demonstrated by altering the pump configuration. Due to the uniform geometry of the BIC cavity, spatially separated multiple vortex beams can also be obtained by exciting the metasurface with multiple pumping beams[268]. These multimode vortex beam lasing show the possibilities for spatial multiplexing.

4.2 Optical sensing

Optical sensors are powerful analytical tools that detect molecules by monitoring changes in optical signals. The most common type is refractometry sensors, which measure the shift of resonance wavelengths induced by changes in the refractive index of the surrounding medium, because it enables simple and label-free detection, significantly enhances the efficiency for real-time detection of molecules at the sensor surface. The overall performance of optical sensors is characterized by a set of parameters including sensitivity (S), figures of merit (FOM) and detection limit (DL). High sensitivity, high figure of merit and low detection limit are desired. The current major challenges for optical sensors are pushing towards single-molecule detection limit and high-throughput detection for practical use. In order to accomplish this, optical resonances should be designed to have both high-Q and large sensing modality simultaneously, which are unique advantages of BIC resonances.

One of the first attempts of utilizing BIC resonances in sensing was led by Romano et al. in 2018, in which the dielectric metasurface made of Si_3N_4 film on SiO_2 substrates was integrated into microfluidic chamber[45]. The BIC resonance in visible range with high Q-factor of ~2000 enables a bulk sensitivity of ~178 nm/RIU and FOM of ~445 for the detection of biphenyl-4-thiol (BPT) with ultralow molecular weight of 186 Da. The idea was then extended to IR range, where the detection of biomolecules such as breast cancer biomarker[52], antigen/antibody[43], peptide nucleic acids, DNA[44] and exosome secretion from single cells[53] is successfully achieved with high sensitivity of up to ~720 nm/RIU, high FOM of ~677 and low DL down to ~4×10^{-7} or 0.2 molecule/mm^2. Moreover, for certain designs, high-order BIC modes such as second-order mode, toroidal dipole and electric quadrupole resonances can outperform the fundamental ones. The larger Q-factor of these high-order BICs leading to the improved sensitivity, FOM and lower the DL of molecules[47,51]. Besides refractometry sensing, small changes in the refractive index also leads to the significant phase jump around the BIC singularity that can be used for sensing[269,270].

A more challenging problem arises when the sensing environment is not spatially and optically homogeneous such as live cells. Romano et al. developed the fluorescence imaging method, where the inhomogeneous fluorescence intensity profile over the metasurface area is correlated with the refractive index map and finally merged with the optical image. The resultant image shows finer details of the cell with a resolution of ~10^{-5} RIU for femtoliter volume of PC3 cell[46]. Scaling up from single-pixel to multi-pixel sensors, Yesilkoy et al. developed an ultrasensitive label-free sensors using a hyperspectral imaging technique that provides high-throughput digital sensing information and allows for multiplexed analyte detection in one measurement[50]. The idea is to design a multi-resonance sensor comprising a series of metasurfaces with tunable high-Q BIC resonance wavelengths λ_i. The mismatch between λ_i and a fixed probe wavelength λ_{probe} determines the characteristic intensity map for different analytes. The intensity map is correlated to pixel in a CMOS camera and encoded into a barcode and decoded using hyperspectral decoder, which maps the spectral information from each CMOS pixel to refractive index. By using this method, the authors obtained information from molecules without using spectrometers or mechanical

scanning.

The use of high-Q BIC resonances for label-free biosensors is still at the preliminary stage, but it presents promising opportunities in the field of chemical and biological detection. However, in order to consistently attain high performance, the fabrication of the high Q-factor metasurfaces approaching theoretical limit should be more reproducible, since Q-factors of BICs are sensitive to fabrication imperfection as well as structural parameters. The choice of materials also plays an important roles. While high-refractive-index dielectric metasurfaces produce high-Q and well-confined field inside the structures, metallic nanostructures are lossy but strong field extended into the sensing media. Hybrid dielectric-metallic metasurfaces can be a direction to leverage the advantages of both materials[271].

Furthermore, a large area of high-Q metasurface needs to be fabricated in a low-cost, high reproducibility and time-effective methodology. The structures fabricated by soft nanoimprinting lithography and reactive ion etching can achieve the sensitivity of up to ~1703 nm/RIU and the FOM of ~65.5[54]. To date, the performance of BIC-based sensors has been mostly demonstrated for simple analytes. The major bottleneck in optical sensing is the investigation of complex biological samples, such as blood, urine, cells, protein molecules and DNA where the media are not spatially and optically homogeneous, that if solved, will lead to significant advances in the field of biomedical research and diagnosis. Anti-interference strategies of BIC sensors for complex real samples have only recently begun to be explored. In particular, pixelated BIC metasurfaces have been proposed as a promising route for complex sample imaging, where spatially resolved quasi-BIC pixels are combined with hyperspectral or digital barcoding readout to retrieve local refractive-index maps in heterogeneous media[50,55,272]. Each pixel support a high-Q quasi-BIC resonance with desired properties such as wavelength and polarization, controlled via geometrical parameters. Optical crosstalk between adjacent pixels originating from evanescent coupling or overlapping far-field scattering, can be mitigated by introducing sub-wavelength isolation trenches, increasing pixel periodicity, or assigning orthogonal polarization states or symmetry-protected BIC modes to neighboring pixels so that a resonance shift in one pixel is not detected in others. Residual cross-interference and illumination non-uniformities can then be further compensated by machine-learning-assisted decoding, where a deep neural network is trained to deconvolve the spectral response of each pixel from the multiplexed intensity map, which has been shown to significantly improve accuracy for heterogeneous biological samples.

4.3 Nonlinear optics

Nonlinear optics describes how intense light interacts with a medium, particularly how the polarization density depends on the electric field[273]. To enable a nonlinear optical mixing process, the frequencies (ω) and phases (φ) of the input waves and output wave have to match, i.e. $\sum \omega_{\rm out} = \sum \omega_{\rm in}$ and $\sum \varphi_{\rm out} = \sum \varphi_{\rm in}$. For metasurfaces or photonic crystals, the phase-matching condition can be relaxed. In order to improve the nonlinear signals, the metasurfaces are generally designed such that the electric field distribution and the pump overlap spatially, while ensuring that the optical modes match with both the excitation and harmonic wavelengths simultaneously. The optimal condition is achieved when the radiative and non-radiative losses are equal, i.e. $Q_{\rm r} = Q_{\rm nr}$[57].

The potential of BIC cavities has been realized across a wide range of materials for second harmonic generation (SHG), third harmonic generation (THG) and high harmonic generation (HHG), with orders of magnitude enhancement compared with a pure film. For example, at the single-particle level, Mie-BIC modes lead to two orders of magnitude enhancement of SHG using a single AlGaAs nanodisk[274], whereas by using high-order Mie mode, SHG conversion efficiency of 1.3×10^{-6} W^{-1} have been achieved, which is two orders of magnitude higher than other types of optical resonances[69]. On the other hand, using BIC metasurfaces composed of arrays of nanoantenna can boost the SHG coefficients to 10^{-4} W^{-1} [275] due to greater flexibility to engineer the optical resonances and Q-factors via more parameters such as pillar size and shape, periodicity, tilting angle and array size. In addition to passive BICs, combining BIC metasurfaces and other materials is a promising route to amplify the advantages from both platforms. The SHG signals could be greatly enhanced by up to two to three orders of magnitude compared with the bare film[75,276,277]. Furthermore, by breaking the centrosymmetry of the nanoparticles, strong SHG signal can be obtained in centrosymmetric materials such as Si[56,61], which is more than two orders of magnitude compared with the metasurfaces made of symmetric Si nanoparticles. The successful demonstration of SHG in Si metasurfaces opens up the possibility of integrating Si photonic devices into optoelectronic circuits. A remarkable achievement is the realization of continuous-wave (cw) SHG using the metasurface of elliptic cylindrical GaP nanoantennas[63]. The SHG signal increases with decreasing the asymmetric parameters. With the obtained Q-factor of ~2000, the SHG signal reaches 2×10^{-7} W^{-1} for the cw pump intensity of 1 kW/cm^2. This result brings metasurface-assisted SHG closer to the demand for cw-SHG.

Quasi-BICs have also shown great potential for enhancing THG by orders of magnitude as demonstrated in various studies on Si metasurfaces by breaking the symmetry of the nanoantenna[57,61,278]. Interestingly, employing multiple-BIC resonance in a single design has shown orders of magnitude enhancement in the efficiency of the nonlinear processes compared with single-BIC design, not limited to

SHG, THG but applicable to four-wave mixing processes[279–282]. The large enhancement of odd harmonic generation up to the 11th order was achieved by satisfying $Q_r = Q_{nr}$ as well as manipulating the near field enhancement via the asymmetry parameter of the metasurfaces. The HHG efficiency and linewidth strongly depend on the temporal profile of the pump; hence, the critical asymmetric parameter for achieving the critical coupling condition $Q_r = Q_{nr}$ is different under different pumping condition[59]. Currently, the record high conversion efficiencies of 3.9×10^{-4} W^{-2} and 4.8×10^{-10} W^{-4} have been reported for THG and fifth-harmonic generation (FHG), respectively by Xiao et al. that will be useful for generation of X-ray and XUV[62].

4.4 Wavefront shaping and Imaging

Nonlocal metasurfaces supporting quasi-BIC resonances provide a versatile framework for wavefront shaping with spectral selectivity and nonlinear imaging, leveraging their high *Q*-factor and strong field localization and the angle-dependent transmission characteristics. Furthermore, this platform strikes an effective balance between local phase modulation governed by individual response of each meta-atom and nonlocal behaviour arising from coupling between meta-atoms, which has been a long-standing challenge for nonlocal meta-lenses. The underlying mechanism is introducing geometric phase to exclusively control the local and nonlocal interactions by spatially tailoring the polarization response of the quasi-BIC resonance, while leaving the non-resonant light unchanged.

In this regard, quasi-BICs exhibit unique advantages to design multifunctional nonlocal metasurfaces by enabling simultaneous control of band structures and narrow-band high-*Q* resonances. A variety of design strategies have been explored theoretically and experimentally to spatially tailor wavefronts at multiple wavelengths, such as applying multiple symmetry perturbations in a single nonlocal metasurfaces[283], and cascading multilayers nonlocal metasurfaces supporting distinct resonant modes[284]. Beyond passive metasurfaces, increasing efforts have focused on actively tunable and reconfigurable metasurfaces. To this end, thermo-optical materials (e.g., TiO_2[285], Si[286]), mechanically stretchable system (e.g., pillars embedded in a flexible matrix[286]), or phase-change material (e.g., Sb_2S_3[287]), whose resonance wavelength shifts with external stimuli such as thermal, mechanical, electrical and optical excitations, can be employed to achieve wavefront shaping at switchable wavelengths.

Enabled by high-*Q* resonances, efficient high-harmonic generation, angular dispersion, inherent polarization vortices, BIC metasurfaces offer multiple degrees of freedom for processing image and optical signals. These capabilities establish BIC metasurfaces as a powerful platform for advanced imaging applications, including nonlinear imaging[288], polarization conversion[289], ultracompact high-pass filters for edge detection and analog optical computing[290–293]. Such BIC-based filters can achieve edge enhancement and spatial differentiation solely through metasurface designs, without the need for bulky or complex optical components, making them highly attractive for miniaturized and integrated imaging systems. Continued progress is anticipated toward achromatic BIC optics and programmable, adaptive imaging platforms. Moreover, the integration of BIC metasurfaces with computational and quantum imaging architectures further represents a promising direction for expanding their functionality and impact.

5 Conclusions and perspectives

5.1 Conclusions

In summary, this Review provides a comprehensive overview of the fundamental mechanisms underlying the formation of different types of BICs and their unique characteristics including ultrahigh *Q*-factors, light trapping and topological properties. Notably, BICs have been demonstrated across a wide range of material systems, covering wavelengths from deep ultraviolet, visible, infrared to microwave. Beyond conventional analytical models and parameter sweeping techniques, inverse design algorithms utilizing iterative methods and machine learning have emerged as powerful tools for designing multifunctional and complex optical nanostructures with improved time- and cost-efficiency, though further improvement is required for on-demand BIC control in more intricate systems.

This Review also delves into the exotic physics enabled by BIC cavities. The ability to manipulate topological charges and system symmetry has led to the realization of super-BICs and chiral BICs, significantly expanding their functionalities. Both extrinsic and intrinsic chiral BICs can generate optical vortex beams in momentum space. Additionally, BIC cavities present exciting opportunities for enhancing light-matter interactions, especially in the realm of single-photon emitters. The demonstration of BIC-polariton condensation and the evanescent coupling of up to 10 BIC-condensates has enabled continuously reprogrammable many-body Hamiltonians in the strong coupling regime. However, despite having theoretically infinite *Q*-factor, BICs experience quadratic decay when moving away from BIC singularities. This limitation can be mitigated by employing super-BIC through merging individual BICs in momentum space or using flatband-BIC via engineering the interactions between photonic modes or Moiré BICs.

Furthermore, BICs hold promise for ultrafast optical phenomena, as their high-*Q* nature makes them highly sensitive to small perturbations in the material properties, enabling rapid and efficient all-optical switching, spectrum conversion and dynamic beam bending. Physics of exceptional point BICs with high *Q* and strong nonlinearity, achieved in non-Hermitian system has shown potential in

various applications due to their higher sensitivity to external perturbation compared to Hermitian systems. Moreover, the integration of active materials into BIC cavities enriches the physics and functional capabilities, unlocking more advanced functionalities and enabling interactions with external factors such as magnetic, electric field and acoustic-optic interactions, fostering the development of dynamic and reconfigurable devices. We also discuss key applications of BIC cavities, including lasing, sensing and nonlinear optics. The combination of BICs with emerging materials has driven paradigm-shifting advancements, offering distinct advantages over conventional photonic cavities and unravelling new opportunities for next-generation optical technologies.

5.2 Perspectives

There remain a great number of exciting challenges and opportunities for further studies on BIC metasurfaces. In this section, we discuss some key challenges for BIC cavities and envision potential solutions and future research directions, spanning fundamental physics, innovative design strategies, advanced fabrication techniques, engineering and enhanced tunability. The ultimate goal is developing practical optical and optoelectronic devices, where BIC cavities play a central role in the operational core.

5.2.1 Fundamental research

While the majority of the previous BIC research focused on single-layer metasurfaces, multilayer BIC metasurfaces offer additional degrees of freedom that can significantly improve the *Q*-factors, field localization and enable controllability over polarization states. In the simplest scenario, a pair of identical metasurfaces can act as meta-mirrors, introducing a phase delay to form a Fabry-Pérot (FP) cavity. In this configuration, the electric field is more strongly confined near the metasurfaces rather than being localized inside the FP cavity[294]. Notably, the *Q*-factors associated with singular points in frequency space can exceed those of traditional FP cavities, despite having shorter cavity lengths. Multilayer metasurfaces also hold significant promise for generating chiral and arbitrarily polarized emissions[155,295]. For instance, by precisely manipulating the spacing between bi-layer metasurfaces, where each individual layer exhibits linear polarization, high-purity chiral emission can be achieved[296]. In the future, BIC or quasi-BIC lasing with arbitrarily polarized emission may become feasible through micro-electromechanical systems (MEMS), enabling precise control of the interlayer distance and twisting angle of bi-layer structures. In another direction, Moiré BIC metasurfaces capable of supporting flatbands with high *Q*-factors over a wide wavevector range could improve coupling efficiency especially with diffusive light sources and provide greater angular control in optoelectronic applications such as light-emitting devices. However, experimental studies of multilayer BIC metasurfaces remain limited, primarily due to the need for multistep lithography with precise nanoscale alignment. Patterning metasurfaces on two sides of a substrate[297], or embedded nanostructures in a cladding layer[298] have been proposed that often lead to compromised performance due to the reduced the index-contrast between the meta-atoms and surrounding environment, optical losses and unwanted scattering. Very recently, two-step electron beam lithography followed by selective development process have demonstrated the feasibility of free-standing stacked bilayer TiO_2 metasurfaces[299]. Overcoming these challenges will inspire more innovative designs for high-performance photonic cavities. For scalable Moiré BIC metasurfaces, large-scale and low-cost fabrication techniques for 3D metasurfaces such as nanoimprint lithography[300], self-assembled colloidal crystals[301] or high-resolution 3D printing via two-photon polymerization[302] could offer promising routes. To extend the library of compatible materials with these methods, critical factors such as material quality, controllable domain size, chemical, thermal and mechanical stability should be engineered on demands. Motivated by the recent achievement of strong coupling between BIC photon and single-photon emitters at elevated temperatures[205], the integration of multiple quantum emitters with BIC cavities will represent a major milestone in quantum photonics. Such systems could unlock a range of quantum phenomena including quantum entanglement, subradiance and superradiance at elevated temperatures, paving the way toward scalable quantum technologies. A key advantage of BIC cavities lies in their high *Q*-factor and large mode volume with field hotspots distributed across the metasurfaces, offering multiple active sites for positioning quantum emitters. The primary challenge remains the deterministic positioning of *indistinguishable* quantum emitters in a cavity. The fabrication must ensure the long coherence time, long-term memory and high-fidelity operation. While atomic force microscope indentation and electron beam irradiation have demonstrated their potential in generating arrays of quantum emitters in van der Waals materials[303,304], the generated emitters have varying characteristics (emission wavelength, polarization, spin). Further effort along the line of developing advanced fabrication methods will be critical to establish the entanglement between two or more cavity quantum electrodynamics (cQED) units that, subsequently, can be integrated into a more complex quantum system. An alternative route is via BIC polariton condensation, where polaritons condensate into the same quantum state, resembling quantum systems. The realization of polariton lasers and Bose-Einstein condensates have inspired a range of applications in quantum information processing and quantum optics, including polariton simulators, neuromorphic computing and polariton qubits[305,306]. In this regard, BIC polaritons offer big advantages in scalable quantum photonic applications due to their long lifetime inherited from the BIC photons that promotes long-range propagation and long-

range interaction between BIC polaritons.

Last but not least, the concept of BIC polaritons is not only limited to excitons but can be extended to other quasi-particles such as phonons, magnons and polarons that are fundamentally interesting. Another promising direction lies in the development of dynamically tunable BIC metasurfaces using novel material platforms that will be beneficial for modulators and photodetectors. Achieving active control on the BIC resonances postfabrication is crucial for realizing reconfigurable BIC devices. Phase-change materials, such as vanadium dioxide[307], antimony trisulfide[308,309], halide perovskites[310] with temperature-dependent refractive indices when transitioning between phases, and electro-optic materials, such as lithium niobate[311], are potential candidates. Alternatively, 2D transition metal dichalcogenide materials provide a promising material platform to electrically control the BIC resonances in energy and momentum space via their charge density[312]. Current challenge to be resolved is their low *Q*-factor attributed to the material surface quality after fabrication or after phase transition. Additionally, embedding liquid crystals, whose refractive indices depend on the alignment of LC molecules, into metasurfaces provides a versatile route for tuning resonance wavelength and polarization state through external electric field[313]. These tunable platforms could play a key role in the next-generation optical devices such as programmable optics, tunable lasers, tunable filters and optoelectronic modulators.

5.2.2 Advanced fabrication techniques

Despite the promising potential of optical BIC cavities, the scalability and practical deployment in realistic photonic applications remain constrained by current limitations in nanofabrication technology. Realizing ultrahigh *Q*-factors in a consistent and reproducible manner demands fabrication processes with nanometer precision, ensuring that the fabricated geometries precisely match the theoretical designs. This challenge becomes particularly critical for quasi-BICs, where structural asymmetries are deliberately introduced to turn BICs into quasi-BICs, whose *Q*-factors are strongly sensitive to fabrication imperfections. Indeed, at the current stage, *Q*-factors of quasi-BIC cavities are experimentally determined to be in a broad range between 10^2 and 10^4, leading to inconsistent performance of BIC devices reported in the literature.

Currently, most metasurfaces are fabricated using conventional lithography techniques followed by reactive-ion etching. While being effective for two-dimensional designs, these techniques face limitations when being applied to multilayer metasurfaces (e.g., PT symmetry, Moiré metasurfaces), structures with broken vertical symmetry or with multi-height profiles that will open a plethora of possibility for design BIC with peculiar functions. The primary challenge is achieving precise alignment across multiple lithography steps, as well as ensuring material compatibility throughout the fabrication process. Addressing these constraints calls for the development of novel fabrication strategies beyond the standard procedure of using electron-beam lithography and dry-etching. For instance, slanted etching methods[101] and multi-step lithography processes[159] have been demonstrated for the fabrication of vertical-symmetry broken metastructures to realize chiral quasi-BICs. Alternatively, 3D laser printing may offer advantages, providing greater degrees of freedom for building multifunctional BIC devices. The development of a low-heat temperature fabrication process or etchless approach will be also necessary to integrate metasurface with active soft materials, such as 2D materials or colloidal quantum dots or directly fabricate metasurface from these material platforms. Overcoming these obstacles will be crucial for unlocking the full potential of BIC-based photonic systems in next-generation optical technologies.

Finally, to extend beyond the lab scale, advancing scalable nanopatterning techniques, which are compatible with industrial standards, is essential. Photolithography methods utilizing interference of UV photons, deep UV and extreme UV can meet the deep-subwavelength resolution demands for wafer-scale production, but at very high operational cost especially for very large area patterning. Soft lithography approaches such as nanoimprint lithography, colloidal lithography could be promising alternatives. Towards commercialization, numerous issues should be fully addressed to ensure defect-free high-resolution patterning, fabrication of complex 3D nanostructures and compatibility with complementary metal-oxide semiconductor (CMOS) technology.

5.2.3 BIC metadevices

BICs offer exceptional promise for next-generation devices, owing to their extraordinary performance demonstrated in low-threshold lasers, vortex microlasers, high-sensitivity low-detection-limit sensors, photonic integrated circuits, ultrafast optical switching, high-dimensional communication and quantum photonic interfaces for strong light-matter interaction at the single-photon level. Realizing these opportunities requires thoughtful designs that account for the material compatibility and the integration of metasurface with active electronic layers to optimize both photonic and electronic performance. While critical challenges remain to be overcome, BICs will continue to be an active and rapidly evolving research area, with immense potential in future applications. We anticipate that many exciting developments in optics and photonics lie ahead, with BICs well positioned to play a central role in shaping that future.

References

1. von Neuman J, Wigner E. Uber merkwürdige diskrete Eigenwerte. Uber das Verhalten von Eigenwerten bei adiabatischen Prozessen. *Phys Z* **30**, 467–470 (1929).
2. Herrick DR. Construction of bound states in the continuum for

epitaxial heterostructure superlattices. *Phys B+C* **85**, 44–50 (1976).
3. Stillinger FH. Potentials supporting positive-energy eigenstates and their application to semiconductor heterostructures. *Phys B+C* **85**, 270–276 (1976).
4. Capasso F, Sirtori C, Faist J et al. Observation of an electronic bound state above a potential well. *Nature* **358**, 565–567 (1992).
5. Deriy I, Toftul I, Petrov M et al. Bound states in the continuum in compact acoustic resonators. *Phys Rev Lett* **128**, 084301 (2022).
6. Huang LJ, Jia B, Kei Y et al. Topological supercavity resonances in the finite system. *Adv Sci* **9**, 2200257 (2022).
7. Marinica DC, Borisov AG, Shabanov SV. Bound states in the continuum in photonics. *Phys Rev Lett* **100**, 183902 (2008).
8. Bulgakov EN, Sadreev AF. Bound states in the continuum in photonic waveguides inspired by defects. *Phys Rev B* **78**, 075105 (2008).
9. Plotnik Y, Peleg O, Dreisow F et al. Experimental observation of optical bound states in the continuum. *Phys Rev Lett* **107**, 183901 (2011).
10. Hsu CW, Zhen B, Lee J et al. Observation of trapped light within the radiation continuum. *Nature* **499**, 188–191 (2013).
11. Muhammad N, Chen Y, Qiu CW et al. Optical bound states in continuum in MoS_2-based metasurface for directional light emission. *Nano Lett* **21**, 967–972 (2021).
12. Wang WH, You B. Symmetry-protected bound states in the continuum in graphene nanoribbons. *J Opt* **24**, 055001 (2022).
13. Zong XY, Li LX, Liu YF. Bound states in the continuum in all-van der Waals photonic crystals: a route enabling electromagnetically induced transparency. *Opt Express* **30**, 17897–17908 (2022).
14. Huang ZJ, Wang MJ, Li Y et al. Highly efficient second harmonic generation of thin film lithium niobate nanograting near bound states in the continuum. *Nanotechnology* **32**, 325207 (2021).
15. Zhao C, Hu GW, Chen Y et al. Unidirectional bound states in the continuum in Weyl semimetal nanostructures. *Photonics Res* **10**, 1828–1838 (2022).
16. Cerjan A, Jürgensen M, Benalcazar WA et al. Observation of a higher-order topological bound state in the continuum. *Phys Rev Lett* **125**, 213901 (2020).
17. Benalcazar WA, Cerjan A. Bound states in the continuum of higher-order topological insulators. *Phys Rev B* **101**, 161116 (2020).
18. Hu ZC, Bongiovanni D, Jukić D et al. Nonlinear control of photonic higher-order topological bound states in the continuum. *Light Sci Appl* **10**, 164 (2021).
19. Wang Y, Xie BY, Lu YH et al. Quantum superposition demonstrated higher-order topological bound states in the continuum. *Light Sci Appl* **10**, 173 (2021).
20. Kodigala A, Lepetit T, Gu Q et al. Lasing action from photonic bound states in continuum. *Nature* **541**, 196–199 (2017).
21. Hsu CW, Zhen B, Stone AD et al. Bound states in the continuum. *Nat Rev Mater* **1**, 16048 (2016).
22. Azzam SI, Kildishev AV. Photonic bound states in the continuum: from basics to applications. *Adv Opt Mater* **9**, 2001469 (2021).
23. Joseph S, Pandey S, Sarkar S et al. Bound states in the continuum in resonant nanostructures: an overview of engineered materials for tailored applications. *Nanophotonics* **10**, 4175–4207 (2021).
24. Xu GZ, Xing HY, Xue ZQ et al. Recent advances and perspective of photonic bound states in the continuum. *Ultrafast Sci* **3**, 0033 (2023).
25. Kang M, Liu T, Chan CT et al. Applications of bound states in the continuum in photonics. *Nat Rev Phys* **5**, 659–678 (2023).
26. Zeng YX, Zhang XD, Ouyang X et al. Manipulating light with bound states in the continuum: from passive to active systems. *Adv Opt Mater* **12**, 2400296 (2024).
27. Koshelev KL, Sadrieva ZF, Shcherbakov AA et al. Bound states in the continuum in photonic structures. *Phys Usp* **66**, 494–517 (2023).
28. Aigner A, Tittl A, Wang J et al. Plasmonic bound states in the continuum to tailor light-matter coupling. *Sci Adv* **8**, eadd4816 (2022).
29. Meudt M, Bogiadzi C, Wrobel K et al. Hybrid photonic–plasmonic bound states in continuum for enhanced light manipulation. *Adv Opt Mater* **8**, 2000898 (2020).
30. Overvig AC, Malek SC, Carter MJ et al. Selection rules for quasi-bound states in the continuum. *Phys Rev B* **102**, 035434 (2020).
31. Refractive index database. Preprint at https://refractiveindex.info/.
32. Chen MH, Xing D, Su VC et al. GaN ultraviolet laser based on bound states in the continuum (BIC). *Adv Opt Mater* **11**, 2201906 (2023).
33. Zhang C, Nie XM, Liu ZT et al. High resolution UV spectral imaging and bio-detection with magnetic dipole quasi-BIC resonant dielectric metasurfaces. *Opt Commun* **530**, 129173 (2023).
34. Kowal D, Wong LJ, Birowosuto MD. Large-area photonic bound state in the continuum for ultraviolet and deep-blue emission for organic, inorganic, and perovskite scintillators. *IEEE Trans Nucl Sci* **70**, 1318–1324 (2023).
35. Wu MF, Ha ST, Shendre S et al. Room-temperature lasing in colloidal nanoplatelets via mie-resonant bound states in the continuum. *Nano Lett* **20**, 6005–6011 (2020).
36. Wu MF, Ding L, Sabatini RP et al. Bound state in the continuum in nanoantenna-coupled slab waveguide enables low-threshold quantum-dot lasing. *Nano Lett* **21**, 9754–9760 (2021).
37. Ruan YH, Li YK, Hu ZD et al. Strong resonance response with ultrahigh quality factor in grating-multilayer systems based on quasi-bound states in the continuum. *Sci Rep* **12**, 21471 (2022).
38. Kühner L, Sortino L, Tilmann B et al. High‐*Q* nanophotonics over the full visible spectrum enabled by hexagonal boron nitride metasurfaces. *Adv Mater* **35**, 2209688 (2023).
39. Wu J, Qing YM. Strong coupling of excitons in patterned few-layer WS_2 with guided mode and bound state in the continuum. *Phys Chem Chem Phys* **24**, 23382–23390 (2022).
40. Weber T, Kühner L, Sortino L et al. Intrinsic strong light-matter coupling with self-hybridized bound states in the continuum in van der Waals metasurfaces. *Nat Mater* **22**, 970–976 (2023).
41. Shen FH, Liu DY, Chen ZF et al. Manipulating the intrinsic light–matter interaction with high- *Q* resonances in an etch-free van der Waals metasurface. *Optica* **12**, 1702–1711 (2025).
42. Ha ST, Paniagua‐Domínguez R, Kuznetsov AI. Room‐temperature multi‐beam, multi‐wavelength bound states in the continuum laser. *Adv Opt Mater* **10**, 2200753 (2022).
43. Romano S, Zito G, Lara Yépez SN et al. Tuning the exponential sensitivity of a bound-state-in-continuum optical sensor. *Opt Express* **27**, 18776–18786 (2019).
44. Zito G, Sanità G, Alulema BG et al. Label-free DNA biosensing by topological light confinement. *Nanophotonics* **10**, 4279–4287 (2021).
45. Romano S, Zito G, Torino S et al. Label-free sensing of ultralow-weight molecules with all-dielectric metasurfaces supporting bound states in the continuum. *Photonics Res* **6**, 726–733 (2018).
46. Romano S, Mangini M, Penzo E et al. Ultrasensitive surface refractive index imaging based on quasi-bound states in the continuum. *ACS Nano* **14**, 15417–15427 (2020).
47. Wang J, Kühne J, Karamanos T et al. All-dielectric crescent metasurface sensor driven by bound states in the continuum. *Adv Funct Mater* **31**, 2104652 (2021).
48. Dang NHM, Gerace D, Drouard E et al. Tailoring dispersion of room-temperature exciton-polaritons with perovskite-based subwavelength metasurfaces. *Nano Lett* **20**, 2113–2119 (2020).
49. Dang NHM, Zanotti S, Drouard E et al. Realization of polaritonic

topological charge at room temperature using polariton bound states in the continuum from perovskite metasurface. *Adv Opt Mater* **10**, 2102386 (2022).
50. Yesilkoy F, Arvelo ER, Jahani Y et al. Ultrasensitive hyperspectral imaging and biodetection enabled by dielectric metasurfaces. *Nat Photonics* **13**, 390–396 (2019).
51. Hsiao HH, Hsu YC, Liu AY et al. Ultrasensitive refractive index sensing based on the quasi‐bound states in the continuum of all‐dielectric metasurfaces. *Adv Opt Mater* **10**, 2200812 (2022).
52. Wang YF, Ali A, Chow EKC et al. An optofluidic metasurface for lateral flow-through detection of breast cancer biomarker. *Biosens Bioelectron* **107**, 224–229 (2018).
53. Ndao A, Hsu L, Cai W et al. Differentiating and quantifying exosome secretion from a single cell using quasi-bound states in the continuum. *Nanophotonics* **9**, 1081–1086 (2020).
54. Zhao HJ, Cao XY, Dong Q et al. Large-area silicon photonic crystal supporting bound states in the continuum and optical sensing formed by nanoimprint lithography. *Nanoscale Adv* **5**, 1291–1298 (2023).
55. Tittl A, Leitis A, Liu MK et al. Imaging-based molecular barcoding with pixelated dielectric metasurfaces. *Science* **360**, 1105–1109 (2018).
56. Fang CZ, Yang QY, Yuan QC et al. Efficient second‐harmonic generation from silicon slotted nanocubes with bound states in the continuum. *Laser Photonics Rev* **16**, 2100498 (2022).
57. Koshelev K, Tang YT, Li KF et al. Nonlinear metasurfaces governed by bound states in the continuum. *ACS Photonics* **6**, 1639–1644 (2019).
58. Yang GC, Dev SU, Allen MS et al. Optical bound states in the continuum enabled by magnetic resonances coupled to a mirror. *Nano Lett* **22**, 2001–2008 (2022).
59. Zograf G, Koshelev K, Zalogina A et al. High-harmonic generation from resonant dielectric metasurfaces empowered by bound states in the continuum. *ACS Photonics* **9**, 567–574 (2022).
60. Shi T, Deng ZL, Geng GZ et al. Planar chiral metasurfaces with maximal and tunable chiroptical response driven by bound states in the continuum. *Nat Commun* **13**, 4111 (2022).
61. Liu ZJ, Xu Y, Lin Y et al. High-*Q* quasibound states in the continuum for nonlinear metasurfaces. *Phys Rev Lett* **123**, 253901 (2019).
62. Xiao SY, Qin MB, Duan JY et al. Robust enhancement of high-harmonic generation from all-dielectric metasurfaces enabled by polarization-insensitive bound states in the continuum. *Opt Express* **30**, 32590–32599 (2022).
63. Anthur AP, Zhang HZ, Paniagua-Dominguez R et al. Continuous wave second harmonic generation enabled by quasi-bound-states in the continuum on gallium phosphide metasurfaces. *Nano Lett* **20**, 8745–8751 (2020).
64. Camacho-Morales R, Xu L, Zhang HZ et al. Sum-frequency generation in high-Q GaP metasurfaces driven by leaky-wave guided modes. *Nano Lett* **22**, 6141–6148 (2022).
65. Ha ST, Fu YH, Emani NK et al. Directional lasing in resonant semiconductor nanoantenna arrays. *Nat Nanotechnol* **13**, 1042–1047 (2018).
66. Mylnikov V, Ha ST, Pan ZY et al. Lasing action in single subwavelength particles supporting supercavity modes. *ACS Nano* **14**, 7338–7346 (2020).
67. Liu L, Wang RX, Zhao XY et al. Heterogeneously integrated quantum-dot emitters efficiently driven by a quasi-BIC-supporting dielectric nanoresonator. *Photonics Res* **10**, 1971–1977 (2022).
68. Ardizzone V, Riminucci F, Zanotti S et al. Polariton Bose–Einstein condensate from a bound state in the continuum. *Nature* **605**, 447–452 (2022).
69. Koshelev K, Kruk S, Melik-Gaykazyan E et al. Subwavelength dielectric resonators for nonlinear nanophotonics. *Science* **367**, 288–292 (2020).
70. Hwang MS, Lee HC, Kim KH et al. Ultralow-threshold laser using super-bound states in the continuum. *Nat Commun* **12**, 4135 (2021).
71. Vincenti MA, Gao J, Frantz JA et al. Third-order nonlinear processes in lossy chalcogenide metasurfaces supporting quasi-bound states in the continuum. In *2022 Sixteenth International Congress on Artificial Materials for Novel Wave Phenomena (Metamaterials)* X-478–X-480 (IEEE, 2022). http://doi.org/10.1109/Metamaterials54993.2022.9920857.
72. Leitis A, Tittl A, Liu MK et al. Angle-multiplexed all-dielectric metasurfaces for broadband molecular fingerprint retrieval. *Sci Adv* **5**, eaaw2871 (2019).
73. Sun KL, Sun M, Cai YJ et al. Strong coupling between quasi-bound states in the continuum and molecular vibrations in the mid-infrared. *Nanophotonics* **11**, 4221–4229 (2022).
74. Liu XY, Liu Y, Fang CZ et al. High-Q resonance in GeSn-based bound states in the continuum microcavity. *Appl Opt* **59**, 10093–10101 (2020).
75. Zhang XT, He LY, Gan X et al. Quasi‐bound states in the continuum enhanced second‐harmonic generation in thin‐film lithium niobate. *Laser Photonics Rev* **16**, 2200031 (2022).
76. Tan TC, Srivastava YK, Ako RT et al. Active control of nanodielectric‐induced THz Quasi‐BIC in flexible metasurfaces: a platform for modulation and sensing. *Adv Mater* **33**, 2100836 (2021).
77. Sun GC, Wang Y, Li YH et al. Tailoring topological nature of merging bound states in the continuum by manipulating structure symmetry of the all-dielectric metasurface. *Phys Rev B* **109**, 035406 (2024).
78. Wang WH, Srivastava YK, Tan TC et al. Brillouin zone folding driven bound states in the continuum. *Nat Commun* **14**, 2811 (2023).
79. Fan JX, Li ZL, Xue ZQ et al. Hybrid bound states in the continuum in terahertz metasurfaces. *Opto-Electron Sci* **2**, 230006 (2023).
80. Cui JY, Chua Y, Han S et al. Single‐mode electrically pumped terahertz laser in an ultracompact cavity via merging bound states in the continuum. *Laser Photonics Rev* **17**, 2300350 (2023).
81. Kupriianov AS, Xu Y, Sayanskiy A et al. Metasurface engineering through bound states in the continuum. *Phys Rev Appl* **12**, 014024 (2019).
82. Joannopoulos JD, Johnson SG, Winn JN et al. *Photonic Crystals: Molding the Flow of Light* 2nd ed (Princeton University Press, Princeton, 2011).
83. Yang Y, Peng C, Liang Y et al. Analytical perspective for bound states in the continuum in photonic crystal slabs. *Phys Rev Lett* **113**, 037401 (2014).
84. Liu WZ, Liu W, Shi L et al. Topological polarization singularities in metaphotonics. *Nanophotonics* **10**, 1469–1486 (2021).
85. Chen WJ, Chen YT, Liu W. Singularities and poincaré indices of electromagnetic multipoles. *Phys Rev Lett* **122**, 153907 (2019).
86. Seo IC, Kim S, Woo BH et al. Fourier-plane investigation of plasmonic bound states in the continuum and molecular emission coupling. *Nanophotonics* **9**, 4565–4577 (2020).
87. Solodovchenko N, Samusev K, Bochek D et al. Bound states in the continuum in strong-coupling and weak-coupling regimes under the cylinder – ring transition. *Nanophotonics* **10**, 4347–4355 (2021).
88. Friedrich H, Wintgen D. Interfering resonances and bound states in the continuum. *Phys Rev A* **32**, 3231–3242 (1985).
89. Lee SG, Kim SH, Kee CS. Bound states in the continuum (BIC) accompanied by avoided crossings in leaky-mode photonic lattices. *Nanophotonics* **9**, 4373–4380 (2020).
90. Zhen B, Hsu CW, Lu L et al. Topological nature of optical bound states in the continuum. *Phys Rev Lett* **113**, 257401 (2014).

91. Liang Y, Peng C, Sakai K et al. Three-dimensional coupled-wave model for square-lattice photonic crystal lasers with transverse electric polarization: a general approach. *Phys Rev B* **84**, 195119 (2011).
92. Jackson JD. *Classical Electrodynamics* (John Wiley & Sons, 2012).
93. Alaee R, Rockstuhl C, Fernandez-Corbaton I. Exact multipolar decompositions with applications in nanophotonics. *Adv Opt Mater* **7**, 1800783 (2019).
94. Sadrieva Z, Frizyuk K, Petrov M et al. Multipolar origin of bound states in the continuum. *Phys Rev B* **100**, 115303 (2019).
95. Zhang FY, Chu QQ, Wang Q et al. Multiple symmetry protected BIC lines in two dimensional synthetic parameter space. *Nanophotonics* **12**, 2405–2413 (2023).
96. Huang ZT, Chang CY, Chen KP et al. Tunable lasing direction in one-dimensional suspended high-contrast grating using bound states in the continuum. *Adv Photonics* **4**, 066004 (2022).
97. Minkov M, Williamson IAD, Xiao M et al. Zero-index bound states in the continuum. *Phys Rev Lett* **121**, 263901 (2018).
98. Dong T, Liang JJ, Camayd-Muñoz S et al. Ultra-low-loss on-chip zero-index materials. *Light Sci Appl* **10**, 10 (2021).
99. Jin JC, Yin XF, Ni LF et al. Topologically enabled ultrahigh-*Q* guided resonances robust to out-of-plane scattering. *Nature* **574**, 501–504 (2019).
100. Yin XF, Jin JC, Soljačić M et al. Observation of topologically enabled unidirectional guided resonances. *Nature* **580**, 467–471 (2020).
101. Chen Y, Deng HC, Sha XB et al. Observation of intrinsic chiral bound states in the continuum. *Nature* **613**, 474–478 (2023).
102. Zhang XD, Liu YL, Han JC et al. Chiral emission from resonant metasurfaces. *Science* **377**, 1215–1218 (2022).
103. Kang M, Mao L, Zhang SP et al. Merging bound states in the continuum by harnessing higher-order topological charges. *Light Sci Appl* **11**, 228 (2022).
104. Wang QZ, Makarenko M, Burguete Lopez A et al. Advancing statistical learning and artificial intelligence in nanophotonics inverse design. *Nanophotonics* **11**, 2483–2505 (2022).
105. Ma W, Liu ZC, Kudyshev ZA et al. Deep learning for the design of photonic structures. *Nat Photonics* **15**, 77–90 (2021).
106. Molesky S, Lin Z, Piggott AY et al. Inverse design in nanophotonics. *Nat Photonics* **12**, 659–670 (2018).
107. Li ZY, Pestourie R, Lin Z et al. Empowering metasurfaces with inverse design: principles and applications. *ACS Photonics* **9**, 2178–2192 (2022).
108. So S, Badloe T, Noh J et al. Deep learning enabled inverse design in nanophotonics. *Nanophotonics* **9**, 1041–1057 (2020).
109. Lin RH, Alnakhli Z, Li XH. Engineering of multiple bound states in the continuum by latent representation of freeform structures. *Photonics Res* **9**, B96–B103 (2021).
110. Minkov M, Williamson IAD, Andreani LC et al. Inverse design of photonic crystals through automatic differentiation. *ACS Photonics* **7**, 1729–1741 (2020).
111. Ma XZ, Ma Y, Cunha P et al. Strategical deep learning for photonic bound states in the continuum (Laser Photonics Rev. 16(10)/2022). *Laser Photonics Rev* **16**, 2270049 (2022).
112. Huang W, Cao ST, Qu XW et al. Inverse design of metamaterial bound states in the continuum device via coupled mode theory. *IEEE Trans Microw Theory Tech* **72**, 1520–1528 (2024).
113. Gladyshev S, Karamanos TD, Kuhn L et al. Inverse design of all-dielectric metasurfaces with accidental bound states in the continuum. *Nanophotonics* **12**, 3767–3779 (2023).
114. Wang LF, Wang WQ, Dong Q et al. Deep learning enabled inverse design of bound states in the continuum with ultrahigh *Q* factor. *J Opt Soc Am B* **41**, A146–A151 (2024).
115. Chen W, Li YY, Liu YN et al. All‐dielectric SERS metasurface with strong coupling quasi‐BIC energized by transformer‐based deep learning. *Adv Opt Mater* **12**, 2301697 (2024).
116. Gao Y, Chen W, Li FJ et al. Meta‐attention deep learning for smart development of metasurface sensors. *Adv Sci* **11**, 2405750 (2024).
117. Dai QQ, Wang YP, Xu C et al. High‐asymmetry metasurface: a new solution for terahertz resonance via active learning‐augmented diffusion model. *Adv Sci* **13**, e08610 (2026).
118. Wang SF, Liu BW, Wu X et al. Transfer learning empowered multiple‐indicator optimization design for terahertz quasi‐bound state in the continuum biosensors. *Adv Sci* **12**, 2504855 (2025).
119. Ren Q, Lang YX, Dang YJ et al. Deep learning-optimized bilayer metasurface based on robust magnetic dipole coupling for MRI enhancement at 70mT. *Opt Express* **33**, 42617–42629 (2025).
120. Wang FF, Chen Y, Zhang ZX et al. Automatic optimization of miniaturized bound states in the continuum cavity. *Opt Express* **31**, 12384–12396 (2023).
121. Xu HJ, Zhao ZY, Ako RT et al. Periodically tunable dual band terahertz electromagnetically-induced transparency of twisted tetramer metasurface. *Opt Express* **33**, 38127–38138 (2025).
122. Gerasimov VS, Kostyukov AS, Ershov AE et al. Machine learning method for predicting line-shapes of Fano resonances induced by bound states in the continuum. *Sci Rep* **15**, 31187 (2025).
123. Jia CJ, Zhao ZY, Wang J. Polarization dependent bound states in continuum in a tetramer metasurface discovered by random forest algorithm. *Sci Rep* **15**, 28008 (2025).
124. Li WB, Lin H, Jia BH et al. Topology-optimized supercavities supporting optical bound states in the continuum. *J Phys Photonics* **8**, 015004 (2026).
125. Chen H, Li N, Zhao YX et al. Maximizing the chirality of bound states in the continuum by inverse design. *Photonics Res* **13**, 2054–2064 (2025).
126. Wang B, Liu WZ, Zhao MX et al. Generating optical vortex beams by momentum-space polarization vortices centred at bound states in the continuum. *Nat Photonics* **14**, 623–628 (2020).
127. Wang JJ, Shi L, Zi J. Spin hall effect of light via momentum-space topological vortices around bound states in the continuum. *Phys Rev Lett* **129**, 236101 (2022).
128. Abdrabou A, Yuan LJ, Lu WT et al. Parametric dependence of bound states in the continuum: a general theory. *Phys Rev A* **107**, 033511 (2023).
129. Zhang YW, Chen A, Liu WZ et al. Observation of polarization vortices in momentum space. *Phys Rev Lett* **120**, 186103 (2018).
130. Doeleman HM, Monticone F, den Hollander W et al. Experimental observation of a polarization vortex at an optical bound state in the continuum. *Nat Photonics* **12**, 397–401 (2018).
131. Yoda T, Notomi M. Generation and annihilation of topologically protected bound states in the continuum and circularly polarized states by symmetry breaking. *Phys Rev Lett* **125**, 053902 (2020).
132. Zeng YX, Hu GW, Liu KP et al. Dynamics of topological polarization singularity in momentum space. *Phys Rev Lett* **127**, 176101 (2021).
133. Zhang ZY, Lan ZH, Xie YZ et al. Bound topological edge state in the continuum for all-dielectric photonic crystals. *Phys Rev Appl* **16**, 064036 (2021).
134. Huang C, Zhang C, Xiao SM et al. Ultrafast control of vortex microlasers. *Science* **367**, 1018–1021 (2020).
135. Yang JH, Huang ZT, Maksimov DN et al. Low‐threshold bound state in the continuum lasers in hybrid lattice resonance metasurfaces. *Laser Photonics Rev* **15**, 2100118 (2021).
136. Kang M, Zhang SP, Xiao M et al. Merging bound states in the continuum at off-high symmetry points. *Phys Rev Lett* **126**, 117402 (2021).
137. Liu LL, Luo HQ, Lu YH et al. Merging diverse bound states in the

continuum: from intrinsic to extrinsic scenarios. *Opt Express* **32**, 16491–16505 (2024).
138. Warning LA, Miandashti AR, Mccarthy LA et al. Nanophotonic approaches for chirality sensing. *ACS Nano* **15**, 15538–15566 (2021).
139. Both S, Schäferling M, Sterl F et al. Nanophotonic chiral sensing: how does it actually work. *ACS Nano* **16**, 2822–2832 (2022).
140. Coles RJ, Price DM, Dixon JE et al. Chirality of nanophotonic waveguide with embedded quantum emitter for unidirectional spin transfer. *Nat Commun* **7**, 11183 (2016).
141. Lodahl P, Mahmoodian S, Stobbe S et al. Chiral quantum optics. *Nature* **541**, 473–480 (2017).
142. Bliokh KY, Rodríguez-Fortuño FJ, Nori F et al. Spin–orbit interactions of light. *Nat Photonics* **9**, 796–808 (2015).
143. Mun J, Kim M, Yang Y et al. Electromagnetic chirality: from fundamentals to nontraditional chiroptical phenomena. *Light Sci Appl* **9**, 139 (2020).
144. Lininger A, Palermo G, Guglielmelli A et al. Chirality in light–matter interaction. *Adv Mater* **35**, 2107325 (2023).
145. Chen Y, Zhao C, Zhang YZ et al. Integrated molar chiral sensing based on high-*Q* metasurface. *Nano Lett* **20**, 8696–8703 (2020).
146. Koshelev K, Tang YT, Hu ZX et al. Resonant chiral effects in nonlinear dielectric metasurfaces. *ACS Photonics* **10**, 298–306 (2023).
147. Liu QS, Chao MH, Zhang WJ et al. Dual-band chiral nonlinear metasurface supported by quasibound states in the continuum. *Ann Phys* **534**, 2200263 (2022).
148. Mao LB, Cheng PY, Liu K et al. Sieving nanometer enantiomers using bound states in the continuum from the metasurface. *Nanoscale Adv* **4**, 1617–1625 (2022).
149. Mao LB, Liu K, Lian M et al. Bound states in the continuum in all-dielectric metasurface: separation of sub-10 nm enantiomers. *Adv Photonics Res* **3**, 2100280 (2022).
150. Ma T, Tian JK, Li J. Chiroptical resonances with high Q factors driven by quasi bound states in the continuum in all-dielectric metasurface at terahertz frequencies. *Opt Commun* **532**, 129216 (2023).
151. Li JT, Yue Z, Li J et al. Ultra-narrowband terahertz circular dichroism driven by planar metasurface supporting chiral quasi bound states in continuum. *Opt Laser Technol* **161**, 109173 (2023).
152. Liu WZ, Wang B, Zhang YW et al. Circularly polarized states spawning from bound states in the continuum. *Phys Rev Lett* **123**, 116104 (2019).
153. Abdrabou A, Lu YY. Circularly polarized states and propagating bound states in the continuum in a periodic array of cylinders. *Phys Rev A* **103**, 043512 (2021).
154. Wang XH, Wang JJ, Zhao XQ et al. Realizing tunable evolution of bound states in the continuum and circularly polarized points by symmetry breaking. *ACS Photonics* **10**, 2316–2322 (2023).
155. Overvig A, Yu NF, Alù A. Chiral quasi-bound states in the continuum. *Phys Rev Lett* **126**, 073001 (2021).
156. Wu JJ, Xu XT, Su XQ et al. Observation of giant extrinsic chirality empowered by quasi-bound states in the continuum. *Phys Rev Appl* **16**, 064018 (2021).
157. Maslovski SI, Morits DK, Tretyakov SA. Symmetry and reciprocity constraints on diffraction by gratings of quasi-planar particles. *J Opt A: Pure Appl Opt* **11**, 074004 (2009).
158. Gorkunov MV, Antonov AA, Kivshar YS. Metasurfaces with maximum chirality empowered by bound states in the continuum. *Phys Rev Lett* **125**, 093903 (2020).
159. Kühner L, Wendisch FJ, Antonov AA et al. Unlocking the out-of-plane dimension for photonic bound states in the continuum to achieve maximum optical chirality. *Light Sci Appl* **12**, 250 (2023).
160. Gorkunov MV, Antonov AA, Tuz VR et al. Bound states in the continuum underpin near-lossless maximum chirality in dielectric metasurfaces. *Adv Opt Mater* **9**, 2100797 (2021).
161. Tang YH, Liang Y, Yao J et al. Chiral bound states in the continuum in plasmonic metasurfaces. *Laser Photonics Rev* **17**, 2200597 (2023).
162. Kim KH, Kim JR. High-*Q* chiroptical resonances by quasi-bound states in the continuum in dielectric metasurfaces with simultaneously broken in-plane inversion and mirror symmetries. *Adv Opt Mater* **9**, 2101162 (2021).
163. Lv WJ, Qin HY, Su ZP et al. Robust generation of intrinsic C points with magneto-optical bound states in the continuum. *Sci Adv* **10**, eads0157 (2024).
164. Wu JY, Ouyang CM, Ma JJ et al. Reconfigurable BIC‐based intrinsic chiral all‐dielectric terahertz metasurfaces. *Laser Photonics Rev* **19**, e00674 (2025).
165. Wang CQ, Wang R, Cheng XG et al. Passively broadband tunable dual circular dichroism via bound states in the continuum in topological chiral metasurface. *ACS Nano* **18**, 18922–18932 (2024).
166. Li HJ, Zhou HM, Wei GG et al. Photonic spin-selective perfect absorptance on planar metasurfaces driven by chiral quasi-bound states in the continuum. *Nanoscale* **15**, 6636–6644 (2023).
167. Deng HC, Jiang X, Zhang Y et al. Chiral lasing enabled by strong coupling. *Sci Adv* **11**, eads9562 (2025).
168. Jia TX, Jeon Y, Feng L et al. Superchirality induced ultrasensitive chiral detection in high-Q optical cavities. *Opto-Electron Adv* **8**, 250079 (2025).
169. Lipkin DM. Existence of a new conservation law in electromagnetic theory. *J Math Phys* **5**, 696–700 (1964).
170. Tang YQ, Cohen AE. Optical chirality and its interaction with matter. *Phys Rev Lett* **104**, 163901 (2010).
171. Barkaoui H, Du K, Chen YM et al. Merged bound states in the continuum for giant superchiral field and chiral mode splitting. *Phys Rev B* **107**, 045305 (2023).
172. Bulgakov EN, Sadreev AF. Transfer of spin angular momentum of an incident wave into orbital angular momentum of the bound states in the continuum in an array of dielectric spheres. *Phys Rev A* **94**, 033856 (2016).
173. Kang L, Wu YH, Ma XZ et al. High-harmonic optical vortex generation from photonic bound states in the continuum. *Adv Opt Mater* **10**, 2101497 (2022).
174. Zito G, Romano S, Cabrini S et al. Observation of spin-polarized directive coupling of light at bound states in the continuum. *Optica* **6**, 1305–1312 (2019).
175. Sunku SS, Ni GX, Jiang BY et al. Photonic crystals for nano-light in moiré graphene superlattices. *Science* **362**, 1153–1156 (2018).
176. Nguyen HS, Dubois F, Deschamps T et al. Symmetry breaking in photonic crystals: on-demand dispersion from flatband to dirac cones. *Phys Rev Lett* **120**, 066102 (2018).
177. Yi CH, Park HC, Park MJ. Strong interlayer coupling and stable topological flat bands in twisted bilayer photonic Moiré superlattices. *Light Sci Appl* **11**, 289 (2022).
178. Nguyen DX, Letartre X, Drouard E et al. Magic configurations in moiré superlattice of bilayer photonic crystals: almost-perfect flatbands and unconventional localization. *Phys Rev Res* **4**, L032031 (2022).
179. Oudich M, Kong XH, Zhang T et al. Engineered moiré photonic and phononic superlattices. *Nat Mater* **23**, 1169–1178 (2024).
180. Luan HY, Ouyang YH, Zhao ZW et al. Reconfigurable moiré nanolaser arrays with phase synchronization. *Nature* **624**, 282–288 (2023).
181. Wang XY, Liu ZJ, Chen B et al. Experimental demonstration of high-efficiency harmonic generation in photonic Moiré superlattice microcavities. *Nano Lett* **24**, 11327–11333 (2024).
182. Wu ZL, Zheng YB. Moiré chiral metamaterials. *Adv Opt Mater* **5**, 1700034 (2017).

183. Aftenieva O, Schnepf M, Mehlhorn B et al. Tunable circular dichroism by photoluminescent Moiré gratings. *Adv Opt Mater* **9**, 2001280 (2021).
184. Lyu BK, Li Y, Jia QW et al. Manipulating the chirality of Moiré metasurface by symmetry breaking. *Laser Photonics Rev* **17**, 2201004 (2023).
185. Ma RM, Luan HY, Zhao ZW et al. Twisted lattice nanocavity with theoretical quality factor exceeding 200 billion. *Fundam Res* **3**, 537–543 (2023).
186. Huang L, Zhang WX, Zhang XD. Moiré quasibound states in the continuum. *Phys Rev Lett* **128**, 253901 (2022).
187. Zhang TC, Dong KC, Li JC et al. Twisted moiré photonic crystal enabled optical vortex generation through bound states in the continuum. *Nat Commun* **14**, 6014 (2023).
188. Ouyang YH, Luan HY, Zhao ZW et al. Singular dielectric nanolaser with atomic-scale field localization. *Nature* **632**, 287–293 (2024).
189. Qin HY, Chen SH, Zhang WX et al. Optical moiré bound states in the continuum. *Nat Commun* **15**, 9080 (2024).
190. Do TTH, Yuan ZY, Durmusoglu EG et al. Room-temperature lasing at flatband bound states in the continuum. *ACS Nano* **19**, 19287–19296 (2025).
191. Le ND, Bouteyre P, Kheir-Aldine A et al. Super bound states in the continuum on a photonic flatband: concept, experimental realization, and optical trapping demonstration. *Phys Rev Lett* **132**, 173802 (2024).
192. Hopfield JJ. Theory of the contribution of excitons to the complex dielectric constant of crystals. *Phys Rev* **112**, 1555–1567 (1958).
193. Andreani LC, Panzarini G, Gérard JM. Strong-coupling regime for quantum boxes in pillar microcavities: theory. *Phys Rev B* **60**, 13276–13279 (1999).
194. Gerace D, Andreani LC. Quantum theory of exciton-photon coupling in photonic crystal slabs with embedded quantum wells. *Phys Rev B* **75**, 235325 (2007).
195. Imamoglu A, Ram RJ, Pau S et al. Nonequilibrium condensates and lasers without inversion: exciton-polariton lasers. *Phys Rev A* **53**, 4250–4253 (1996).
196. Cueff S, Berguiga L, Nguyen HS. Fourier imaging for nanophotonics. *Nanophotonics* **13**, 841–858 (2024).
197. Cao S, Dong HG, He JL et al. Normal-incidence-excited strong coupling between excitons and symmetry-protected quasi-bound states in the continuum in silicon nitride–WS_2 heterostructures at room temperature. *J Phys Chem Lett* **11**, 4631–4638 (2020).
198. Qin MB, Duan JY, Xiao SY et al. Strong coupling between excitons and quasibound states in the continuum in bulk transition metal dichalcogenides. *Phys Rev B* **107**, 045417 (2023).
199. Koshelev KL, Sychev SK, Sadrieva ZF et al. Strong coupling between excitons in transition metal dichalcogenides and optical bound states in the continuum. *Phys Rev B* **98**, 161113 (2018).
200. Kravtsov V, Khestanova E, Benimetskiy FA et al. Nonlinear polaritons in a monolayer semiconductor coupled to optical bound states in the continuum. *Light Sci Appl* **9**, 56 (2020).
201. Maggiolini E, Polimeno L, Todisco F et al. Strongly enhanced light–matter coupling of monolayer WS_2 from a bound state in the continuum. *Nat Mater* **22**, 964–969 (2023).
202. Berghuis AM, Castellanos GW, Murai S et al. Room temperature exciton–polariton condensation in silicon metasurfaces emerging from bound states in the continuum. *Nano Lett* **23**, 5603–5609 (2023).
203. Wu XX, Zhang S, Song JP et al. Exciton polariton condensation from bound states in the continuum at room temperature. *Nat Commun* **15**, 3345 (2024).
204. Gianfrate A, Sigurðsson H, Ardizzone V et al. Reconfigurable quantum fluid molecules of bound states in the continuum. *Nat Phys* **20**, 61–67 (2024).
205. Do TTH, Nonahal M, Li C et al. Room-temperature strong coupling in a single-photon emitter-metasurface system. *Nat Commun* **15**, 2281 (2024).
206. Biswas SK, Adi W, Beisenova A et al. From weak to strong coupling: quasi-BIC metasurfaces for mid-infrared light–matter interactions. *Nanophotonics* **13**, 2937–2949 (2024).
207. Wang YT, Adamo G, Ha ST et al. Electrically generated exciton polaritons with spin on‐demand. *Adv Mater* **37**, 2412952 (2025).
208. Chai Z, Hu XY, Wang FF et al. Ultrafast all‐optical switching. *Adv Opt Mater* **5**, 1600665 (2017).
209. Guo QS, Sekine R, Ledezma L et al. Femtojoule femtosecond all-optical switching in lithium niobate nanophotonics. *Nat Photonics* **16**, 625–631 (2022).
210. Nelan SP, Mercante A, Shi SY et al. Ultra-high extinction dual-output thin-film lithium niobate intensity modulator. *IEEE Access* **10**, 100300–100311 (2022).
211. Qi HX, Wang XX, Hu XY et al. All-optical switch based on novel physics effects. *J Appl Phys* **129**, 210906 (2021).
212. Fan KB, Shadrivov IV, Padilla WJ. Dynamic bound states in the continuum. *Optica* **6**, 169–173 (2019).
213. Zhong HZ, Liu ZQ, Liu XS et al. Ultra-high quality graphene perfect absorbers for high performance switching manipulation. *Opt Express* **28**, 37294–37306 (2020).
214. Ma WB, Zhou CB, Chen DL et al. Active quasi-BIC metasurfaces assisted by epsilon-near-zero materials. *Opt Express* **31**, 13125–13139 (2023).
215. Karl N, Vabishchevich PP, Liu S et al. All-optical tuning of symmetry protected quasi bound states in the continuum. *Appl Phys Lett* **115**, 141103 (2019).
216. Lemasters R, Shcherbakov MR, Yang GC et al. Deep optical switching on subpicosecond timescales in an amorphous Ge metamaterial. *Adv Opt Mater* **9**, 2100240 (2021).
217. Hu YZ, Tong MY, Hu SY et al. Spatiotemporal lineshape tailoring in BIC‐mediated reconfigurable metamaterials. *Adv Funct Mater* **32**, 2203680 (2022).
218. Ren ZH, Hu YZ, He WB et al. Overcoming high-quality limitations in plasmonic metasurfaces for ultrasensitive terahertz applications. *ACS Nano* **18**, 21211–21220 (2024).
219. Yang YM, Wang WY, Boulesbaa A et al. Nonlinear fano-resonant dielectric metasurfaces. *Nano Lett* **15**, 7388–7393 (2015).
220. Yang GC, Allen MS, Allen JW et al. Unlocking efficient ultrafast bound-electron optical nonlinearities via mirror induced quasi bound states in the continuum. *Nano Lett* **24**, 1679–1686 (2024).
221. Ono M, Hata M, Tsunekawa M et al. Ultrafast and energy-efficient all-optical switching with graphene-loaded deep-subwavelength plasmonic waveguides. *Nat Photonics* **14**, 37–43 (2020).
222. Crotti G, Akturk M, Schirato A et al. Giant ultrafast dichroism and birefringence with active nonlocal metasurfaces. *Light Sci Appl* **13**, 204 (2024).
223. Wu YH, Kang L, Werner DH. Active quasi-BIC optical vortex generators for ultrafast switching. *New J Phys* **24**, 033002 (2022).
224. Karl N, Vabishchevich PP, Shcherbakov MR et al. Frequency conversion in a time-variant dielectric metasurface. *Nano Lett* **20**, 7052–7058 (2020).
225. Berté R, Possmayer T, Tittl A et al. All-optical permittivity-asymmetric *quasi*-bound states in the continuum. *Light Sci Appl* **14**, 185 (2025).
226. Shilkin DA, Ha ST, Paniagua-Domínguez R et al. Ultrafast modulation of a nonlocal semiconductor metasurface under spatially selective optical pumping. *Nano Lett* **24**, 14229–14235 (2024).
227. Shcherbakov MR, Werner K, Fan ZY et al. Photon acceleration and tunable broadband harmonics generation in nonlinear time-dependent metasurfaces. *Nat Commun* **10**, 1345 (2019).
228. Zubyuk VV, Shafirin PA, Shcherbakov MR et al. Externally driven

nonlinear time-variant metasurfaces. *ACS Photonics* **9**, 493–502 (2022).
229. Upham J, Tanaka Y, Asano T et al. Dynamic increase and decrease of photonic crystal nanocavity Q factors for optical pulse control. *Opt Express* **16**, 21721–21730 (2008).
230. Upham J, Fujita Y, Kawamoto Y et al. The capture, hold and forward release of an optical pulse from a dynamic photonic crystal nanocavity. *Opt Express* **21**, 3809–3817 (2013).
231. Upham J, Inoue H, Tanaka Y et al. Pulse capture without carrier absorption in dynamic Q photonic crystal nanocavities. *Opt Express* **22**, 15459–15466 (2014).
232. Shafirin PA, Zubyuk VV, Fedyanin AA et al. Nonlinear response of Q-boosting metasurfaces beyond the time-bandwidth limit. *Nanophotonics* **11**, 4053–4061 (2022).
233. Franceschini P, Tognazzi A, Chernyak AM et al. Enhancing second harmonic generation by Q-boosting lossless cavities beyond the time bandwidth limit. *Nanophotonics* **13**, 1–8 (2024).
234. Otey CR, Povinelli ML, Fan SH. Completely capturing light pulses in a few dynamically tuned microcavities. *J Lightwave Technol* **26**, 3784–3793 (2008).
235. Hayran Z, Monticone F. Capturing broadband light in a compact bound state in the continuum. *ACS Photonics* **8**, 813–823 (2021).
236. Xu QF, Dong P, Lipson M. Breaking the delay-bandwidth limit in a photonic structure. *Nat Phys* **3**, 406–410 (2007).
237. Yang ZW, Liu MK, Smirnova D et al. Ultrafast Q-boosting in semiconductor metasurfaces. *Nanophotonics* **13**, 2173–2182 (2024).
238. Crotti G, Schirato A, Pashina O et al. Ultrafast switching of a metasurface quasi-bound state in the continuum via transient optical symmetry breaking. *Light Sci Appl* **14**, 240 (2025).
239. Aigner A, Possmayer T, Weber T et al. Optical control of resonances in temporally symmetry-broken metasurfaces. *Nature* **644**, 896–902 (2025).
240. Persson E, Rotter I, Stöckmann HJ et al. Observation of resonance trapping in an open microwave cavity. *Phys Rev Lett* **85**, 2478–2481 (2000).
241. Dembowski C, Gräf HD, Harney HL et al. Experimental observation of the topological structure of exceptional points. *Phys Rev Lett* **86**, 787–790 (2001).
242. Solodovchenko NS, Samusev KB, Limonov MF. Quadruplets of exceptional points and bound states in the continuum in dielectric rings. *Phys Rev B* **109**, 075131 (2024).
243. Zhen B, Hsu CW, Igarashi Y et al. Spawning rings of exceptional points out of Dirac cones. *Nature* **525**, 354–358 (2015).
244. Miri MA, Alù A. Exceptional points in optics and photonics. *Science* **363**, eaar7709 (2019).
245. Zhou HY, Peng C, Yoon Y et al. Observation of bulk Fermi arc and polarization half charge from paired exceptional points. *Science* **359**, 1009–1012 (2018).
246. Hodaei H, Hassan AU, Wittek S et al. Enhanced sensitivity at higher-order exceptional points. *Nature* **548**, 187–191 (2017).
247. Chen WJ, Kaya Özdemir Ş, Zhao GM et al. Exceptional points enhance sensing in an optical microcavity. *Nature* **548**, 192–196 (2017).
248. Zhang MN, Dong L, Wang LF et al. Exceptional points enhance sensing in silicon micromechanical resonators. *Microsyst Nanoeng* **10**, 12 (2024).
249. Park JH, Ndao A, Cai W et al. Symmetry-breaking-induced plasmonic exceptional points and nanoscale sensing. *Nat Phys* **16**, 462–468 (2020).
250. Chen WJ, Wang CQ, Peng B et al. Non-hermitian physics and exceptional points in high-quality optical microresonators. In Xiao YF, Zou CL, Gong QH. *Ultra-High-Q Optical Microcavities* 269–313 (World Scientific, Singapore, 2020). doi: 10.1142/9789814566070_0008.
251. Wiersig J. Review of exceptional point-based sensors. *Photonics Res* **8**, 1457–1467 (2020).
252. Ding K, Fang C, Ma GC. Non-Hermitian topology and exceptional-point geometries. *Nat Rev Phys* **4**, 745–760 (2022).
253. Lin Z, Pick A, Lončar M et al. Enhanced spontaneous emission at third-order dirac exceptional points in inverse-designed photonic crystals. *Phys Rev Lett* **117**, 107402 (2016).
254. Pick A, Zhen B, Miller OD et al. General theory of spontaneous emission near exceptional points. *Opt Express* **25**, 12325–12348 (2017).
255. Ferrier L, Bouteyre P, Pick A et al. Unveiling the enhancement of spontaneous emission at exceptional points. *Phys Rev Lett* **129**, 083602 (2022).
256. Lu LR, Le-Van Q, Ferrier L et al. Engineering a light–matter strong coupling regime in perovskite-based plasmonic metasurface: quasi-bound state in the continuum and exceptional points. *Photonics Res* **8**, A91–A100 (2020).
257. Masharin MA, Samusev AK, Bogdanov AA et al. Room‐temperature exceptional‐point‐driven polariton lasing from perovskite metasurface. *Adv Funct Mater* **33**, 2215007 (2023).
258. Qin HY, Shi XD, Ou HY. Exceptional points at bound states in the continuum in photonic integrated circuits. *Nanophotonics* **11**, 4909–4917 (2022).
259. Deng ZL, Li FJ, Li HN et al. Extreme diffraction control in metagratings leveraging bound states in the continuum and exceptional points. *Laser Photonics Rev* **16**, 2100617 (2022).
260. Canós Valero A, Sztranyovszky Z, Muljarov EA et al. Exceptional bound states in the continuum. *Phys Rev Lett* **134**, 103802 (2025).
261. Ren YH, Li PS, Liu ZJ et al. Low-threshold nanolasers based on miniaturized bound states in the continuum. *Sci Adv* **8**, eade8817 (2022).
262. Mermet-Lyaudoz R, Symonds C, Berry F et al. Taming Friedrich–Wintgen interference in a resonant metasurface: vortex laser emitting at an on-demand tilted angle. *Nano Lett* **23**, 4152–4159 (2023).
263. Sadrieva ZF, Sinev IS, Koshelev KL et al. Transition from optical bound states in the continuum to leaky resonances: role of substrate and roughness. *ACS Photonics* **4**, 723–727 (2017).
264. Droulias S, Koschny T, Soukoulis CM. Finite-size effects in metasurface lasers based on resonant dark states. *ACS Photonics* **5**, 3788–3793 (2018).
265. Zhong HC, Yu Y, Zheng ZY et al. Ultra-low threshold continuous-wave quantum dot mini-BIC lasers. *Light Sci Appl* **12**, 100 (2023).
266. Cui JY, Han S, Zhu BF et al. Ultracompact multibound-state-assisted flat-band lasers. *Nat Photonics* **19**, 643–649 (2025).
267. Yu Y, Sakanas A, Zali AR et al. Ultra-coherent Fano laser based on a bound state in the continuum. *Nat Photonics* **15**, 758–764 (2021).
268. Zhai ZS, Li Z, Du YX et al. Multimode vortex lasing from dye–TiO_2 lattices via bound states in the continuum. *ACS Photonics* **10**, 437–446 (2023).
269. Sakotic Z, Krasnok A, Alú A et al. Topological scattering singularities and embedded eigenstates for polarization control and sensing applications. *Photonics Res* **9**, 1310–1323 (2021).
270. Liu ZC, Guo TB, Tan Q et al. Phase interrogation sensor based on all-dielectric BIC metasurface. *Nano Lett* **23**, 10441–10448 (2023).
271. Luo M, Zhou Y, Zhao XY et al. High-sensitivity optical sensors empowered by quasi-bound states in the continuum in a hybrid metal–dielectric metasurface. *ACS Nano* **18**, 6477–6486 (2024).
272. Aigner A, Weber T, Wester A et al. Continuous spectral and coupling-strength encoding with dual-gradient metasurfaces. *Nat Nanotechnol* **19**, 1804–1812 (2024).
273. Boyd R W. *Nonlinear Optics* 3rd ed (Academic Press, Amsterdam,

2008).
274. Carletti L, Koshelev K, De Angelis C et al. Giant nonlinear response at the nanoscale driven by bound states in the continuum. *Phys Rev Lett* **121**, 033903 (2018).
275. Ning TY, Li X, Zhang ZS et al. Ultimate conversion efficiency of second harmonic generation in all-dielectric resonators of quasi-BICs in consideration of nonlinear refraction of dielectrics. *Opt Express* **29**, 17286–17294 (2021).
276. Bernhardt N, Koshelev K, White SJU et al. Quasi-BIC resonant enhancement of second-harmonic generation in WS_2 monolayers. *Nano Lett* **20**, 5309–5314 (2020).
277. Löchner FJF, George A, Koshelev K et al. Hybrid dielectric metasurfaces for enhancing second-harmonic generation in chemical vapor deposition grown MoS_2 monolayers. *ACS Photonics* **8**, 218–227 (2021).
278. Xu L, Zangeneh Kamali K, Huang LJ et al. Dynamic nonlinear image tuning through magnetic dipole quasi‐BIC ultrathin resonators. *Adv Sci* **6**, 1802119 (2019).
279. Wang TC, Zhang XD. Improved third-order nonlinear effect in graphene based on bound states in the continuum. *Photonics Res* **5**, 629–639 (2017).
280. Liu TT, Qin MB, Wu F et al. High-efficiency optical frequency mixing in an all-dielectric metasurface enabled by multiple bound states in the continuum. *Phys Rev B* **107**, 075441 (2023).
281. Ye ZH, Fan YC, Sun KY et al. Dual quasi-bound state enhanced second harmonic generation in lithium niobate metasurfaces. *Opt Quant Electron* **56**, 2002 (2024).
282. Liu TT, Qin MB, Qiu JM et al. Polarization-independent enhancement of third-harmonic generation empowered by doubly degenerate quasi-bound states in the continuum. *Nano Lett* **25**, 3646–3652 (2025).
283. Overvig AC, Malek SC, Yu NF. Multifunctional nonlocal metasurfaces. *Phys Rev Lett* **125**, 017402 (2020).
284. Malek SC, Overvig AC, Alù A et al. Multifunctional resonant wavefront-shaping meta-optics based on multilayer and multi-perturbation nonlocal metasurfaces. *Light Sci Appl* **11**, 246 (2022).
285. Malek SC, Tsai CC, Yu NF. Thermally‐switchable metalenses based on quasi‐bound states in the continuum. *Laser Photonics Rev* **19**, 2300618 (2025).
286. Malek SC, Overvig AC, Shrestha S et al. Active nonlocal metasurfaces. *Nanophotonics* **10**, 655–665 (2020).
287. Liu TT, Zhang DD, Liu WX et al. Phase-change nonlocal metasurfaces for dynamic wave-front manipulation. *Phys Rev Appl* **21**, 044004 (2024).
288. Zheng Z, Smirnova D, Sanderson G et al. Broadband infrared imaging governed by guided-mode resonance in dielectric metasurfaces. *Light Sci Appl* **13**, 249 (2024).
289. Yao J, Lai FX, Fan YB et al. Nonlocal meta-lens with Huygens' bound states in the continuum. *Nat Commun* **15**, 6543 (2024).
290. Liu TT, Qiu JM, Xu L et al. Edge detection imaging by quasi-bound states in the continuum. *Nano Lett* **24**, 14466–14474 (2024).
291. Guo KN, Jiang Y, Xiao SY et al. Tunable edge and depth sensing via phase-change nonlocal metasurfaces. *Phys Rev Appl* **24**, 044005 (2025).
292. Zhang K, Wang S, Qiu JM et al. Momentum‐space tunable metasurfaces for switchable image processing. *Adv Opt Mater* **13**, 2500352 (2025).
293. Zhou C, Zhao RZ, Li PJ et al. Dual‐polarized broadband Laplace differentiator via quasi‐bound states in the continuum empowered by nonlocal metasurfaces. *Adv Funct Mater* **35**, 2426095 (2025).
294. Alagappan G, García-Vidal FJ, Png CE. Fabry-perot resonances in bilayer metasurfaces. *Phys Rev Lett* **133**, 226901 (2024).
295. Qin HY, Su ZP, Liu MQ et al. Arbitrarily polarized bound states in the continuum with twisted photonic crystal slabs. *Light Sci Appl* **12**, 66 (2023).
296. Gromyko D, An S, Gorelik S et al. Unidirectional chiral emission via twisted Bi-layer metasurfaces. *Nat Commun* **15**, 9804 (2024).
297. Groever B, Chen WT, Capasso F. Meta-lens doublet in the visible region. *Nano Lett* **17**, 4902–4907 (2017).
298. Georgi P, Wei QS, Sain B et al. Optical secret sharing with cascaded metasurface holography. *Sci Adv* **7**, eabf9718 (2021).
299. Dorrah AH, Park JS, Palmieri A et al. Free-standing bilayer metasurfaces in the visible. *Nat Commun* **16**, 3126 (2025).
300. Ye JC, Wang YX, Tang ZX et al. Optical metasurface fabricated using 3D nanoimprint lithography. *J Vac Sci Technol B* **42**, 062212 (2024).
301. Cai ZY, Li ZW, Ravaine S et al. From colloidal particles to photonic crystals: advances in self-assembly and their emerging applications. *Chem Soc Rev* **50**, 5898–5951 (2021).
302. Zhang W, Min JK, Wang H et al. Printing of 3D photonic crystals in titania with complete bandgap across the visible spectrum. *Nat Nanotechnol* **19**, 1813–1820 (2024).
303. Xu XH, Martin ZO, Sychev D et al. Creating quantum emitters in hexagonal boron nitride deterministically on chip-compatible substrates. *Nano Lett* **21**, 8182–8189 (2021).
304. Fournier C, Plaud A, Roux S et al. Position-controlled quantum emitters with reproducible emission wavelength in hexagonal boron nitride. *Nat Commun* **12**, 3779 (2021).
305. Kavokin A, Liew TCH, Schneider C et al. Polariton condensates for classical and quantum computing. *Nat Rev Phys* **4**, 435–451 (2022).
306. Liew TCH. The future of quantum in polariton systems: opinion. *Opt Mater Express* **13**, 1938–1946 (2023).
307. Aigner A, Ligmajer F, Rovenská K et al. Engineering of active and passive loss in high-quality-factor vanadium dioxide-based BIC metasurfaces. *Nano Lett* **24**, 10742–10749 (2024).
308. Xie ZY, Li C, Murali K et al. Ultrathin BIC metasurfaces based on ultra-low-loss Sb_2Se_3 phase-change material. *Nano Lett* **25**, 251–260 (2025).
309. Abdelraouf OAM, Wu M, Liu H. Hybrid metasurfaces enabling focused tunable amplified photoluminescence through dual bound states in the continuum. *Adv Funct Mater* **35**, 2505165 (2025).
310. Tian JY, Adamo G, Liu HL et al. Phase‐change perovskite microlaser with tunable polarization vortex. *Adv Mater* **35**, 2207430 (2023).
311. Qiu HF, Tu X, Qin MB et al. Electro-optically tunable second-harmonic generation in lithium niobate metasurfaces boosted by Brillouin zone folding induced bound states in the continuum. *Phys Rev B* **112**, 085418 (2025).
312. Zhao C, Chen WJ, Wei JX et al. Electrically tunable and robust bound states in the continuum enabled by 2D transition metal dichalcogenide. *Adv Opt Mater* **10**, 2201634 (2022).
313. Yu BB, Yang F, Zeng MD et al. Liquid crystal enables extraordinarily precise tunability for a high‐*Q* ultra‐narrowband filter based on a quasi‐BIC metasurface. *Adv Funct Mater* **35**, 2413098 (2025).

Acknowledgements

S. T. H and T. T. H. D acknowledge the financial support from National Research Foundation, Singapore-Frontier Competitive Research Grant (NRF-F-CRP-2024-0009) and A*STAR MTC-Programmatic Fund (M24N9b0122). C. D. and Z. Y. acknowledge funding support from the National Research Foundation

Competitive Research Program (NRF-CRP29-2022-0003), Ministry of Education, Singapore under its AcRF Tier 2 grant (MOE-T2EP50121-0012) and AcRF Tier 1 grant (RG140/23). D. A. S. acknowledges the funding support from A*STAR under Career Development Fund (C243512005). J.T. acknowledges the support from the National Research Foundation, Singapore under NRF-CRP (NRF-CRP26-2021-0004), the Agency for Science, Technology and Research (A*STAR) under MTC Programmatic Grant (M22L1b0110), and the National Semiconductor Translation and Innovation Centre (NSTIC).

Author contributions

All authors commented on the manuscript.

Competing interests

The authors declare no competing financial interests.

Open Access This article is licensed under a Creative Commons Attribution 4.0 International License, which permits use, sharing, adaptation, distribution and reproduction in any medium or format, as long as you give appropriate credit to the original author(s) and the source, provide a link to the Creative Commons license, and indicate if changes were made. To view a copy of this license, visit http://creativecommons.org/licenses/by/4.0/
©The Author(s) 2026.
Published by Editorial Office of *Opto-Electronic Advance*, Institute of Optics and Electronics, Chinese Academy of Sciences.

Opto-Electronic Journals Group
www.oejournal.org
Scan for Article PDF